Cerebral Cortex, 2020;00: 1–19

doi: 10.1093/cercor/bhaa137
Original Article

Downloaded from https://academic.oup.com/cercor/article-abstract/doi/10.1093/cercor/bhaa137/5860958 by University of Canberra user on 25 June 2020

ORIGINAL ARTICLE

COUP-TFI/Nr2f1 Orchestrates Intrinsic Neuronal Activity during Development of the Somatosensory Cortex

Isabel Del Pino[1,4], Chiara Tocco[2], Elia Magrinelli[2,5], Andrea Marcantoni[3], Celeste Ferraguto[2], Giulia Tomagra[3], Michele Bertacchi[2], Christian Alfano[2], Xavier Leinekugel[1], Andreas Frick[1] and Michèle Studer[2,‡]

[1]Université de Bordeaux, Inserm U1215, Neurocentre Magendie, 33077 Bordeaux, France, [2]Université Côte d'Azur, CNRS, Inserm, iBV, 06108 Nice, France, [3]Dipartimento di Scienza e Tecnologia del Farmaco, Università di Torino, 10125 Torino, Italy, [4]Present address: Centro de Investigación Príncipe Felipe, 46012 Valencia, Spain and [5]Present address: Département des Neurosciences Fondamentales, Université de Lausanne, CH-1005 Lausanne, Switzerland

Address correspondence to Michèle Studer, Institut de Biologie Valrose (iBV), Univ. Nice Sophia Antipolis, Centre de Biochimie; UFR Sciences, Parc Valrose, 28 avenue Valrose, 06108 Nice Cedex 2, France. Email: Michele.studer@unice.fr

[†]Isabel del Pino, Chiara Tocco, Elia Magrinelli, and Andrea Marcantoni are co-first authors
[‡]Xavier Leinekugel, Andreas Frick, and Michèle Studer are co-last senior authors

Abstract

The formation of functional cortical maps in the cerebral cortex results from a timely regulated interaction between intrinsic genetic mechanisms and electrical activity. To understand how transcriptional regulation influences network activity and neuronal excitability within the neocortex, we used mice deficient for *Nr2f1* (also known as *COUP-TFI*), a key determinant of primary somatosensory (S1) area specification during development. We found that the cortical loss of *Nr2f1* impacts on spontaneous network activity and synchronization of S1 cortex at perinatal stages. In addition, we observed alterations in the intrinsic excitability and morphological features of layer V pyramidal neurons. Accordingly, we identified distinct voltage-gated ion channels regulated by *Nr2f1* that might directly influence intrinsic bioelectrical properties during critical time windows of S1 cortex specification. Altogether, our data suggest a tight link between *Nr2f1* and neuronal excitability in the developmental sequence that ultimately sculpts the emergence of cortical network activity within the immature neocortex.

Key words: Nr2f1/COUP-TFI, intrinsic excitability, spontaneous activity, layer V pyramidal neurons, somatosensory cortex

Introduction

The area- and cell-type specific organization of the mammalian neocortex is a process involving coordinated interactions between cell intrinsic genetic programs and neural activity, an essential feature in specifying the composition and organization of neural circuits during all stages of development (Jabaudon 2017; Simi and Studer 2018). Before experience shapes neuronal circuits *via* sensory-driven activity, the developing cortex is genetically primed to establish patterns of local spontaneous activity, which autonomously synchronizes large groups of neurons independently of sensory stimulation and contributes to the development of neuronal circuits (Kirischuk et al. 2017; Andreae and Burrone 2018; Luhmann and Khazipov 2018; Anton-Bolanos et al. 2019). These early patterns of spontaneous

© The Author(s) 2020. Published by Oxford University Press. All rights reserved. For permissions, please e-mail: journals.permissions@oup.com

activity are thought to set the initial blueprint of cortical network organization, and their alteration during cortical development leads to the formation of dysfunctional cortical circuits (Kirkby et al. 2013; Li et al. 2013). The embryonic thalamus also conveys spontaneous neuronal activity to the immature cortex, influencing the formation of a functional somatotopic map (Anton-Bolanos et al. 2019). Hence, local spontaneous activity in cortical and precortical relay stations during embryonic and early postnatal stages might prepare cortical areas and circuits for upcoming sensory input.

Spontaneous activity emerging during early development in different cortical areas in form of calcium (Ca^{2+}) waves has been reported already at embryonic day E16 in mice, most probably generated in proliferating radial glia cells (Kirischuk et al. 2017). Immature neurons express voltage-dependent ion channels, responsible for a highly synchronized spontaneous activity within small neuronal networks (Luhmann et al. 2016). Finally, certain features of immature cells, including high membrane resistance and prominent low-threshold calcium currents, seem to enhance excitability in neurons receiving little afferent sensory input (Moody and Bosma 2005).

Besides spontaneous activity, the neocortical primordium is under the control of distinct morphogens that establish proper coordinates along the developing anteroposterior and dorsoventral cortical axes (O'Leary and Sahara 2008; Alfano and Studer 2012; Greig et al. 2013). Functioning in a dose-, context-, and time-dependent manner, these signaling pathways modulate the gradient expression of area patterning genes, such as *Pax6*, *Sp8*, *Emx2*, and *Nr2f1* (also known as *COUP-TFI*), among others. These transcriptional regulators cooperatively instruct cell identity acquisition in cortical progenitors and early postmitotic neurons, building a rough primordial areal map, known as a protomap, which will be refined by sensory-evoked activity during postnatal stages (Simi and Studer 2018; Cadwell et al. 2019). Changes in dosage of these factors alter the size and position of primordial area maps with severe consequences in cell-type specification and circuit formation (Greig et al. 2013; Jabaudon 2017). Although the interaction between cortical patterning genes and onset of spontaneous activity during primary area mapping has been hypothesized, there is still no clear evidence on how this interaction is perpetrated.

To tackle this question, we used mice deficient for the nuclear receptor *Nr2f1*, a gene coding for a member of the superfamily of steroid hormone receptors and a key transcriptional regulator during cortical development, as a genetic model of altered primary somatosensory (S1) area mapping (Armentano et al. 2007). In humans, haploinsufficiency of the *NR2F1* gene leads to an emerging genetic neurodevelopmental disorder, named Bosch-Boonstra-Schaaf Optic Atrophy Syndrome. Patients affected by this autosomal-dominant disorder exhibit several clinical features, such as intellectual disability, epileptic seizures, autistic-like traits, abnormal fine motor coordination, and optic atrophy (Bosch et al. 2014; Chen et al. 2016; Bertacchi et al. 2019). In mice, *Nr2f1* represents a well-studied area patterning gene, which determines sensory identity, controls neuronal migration, and laminar specification; its loss of function leads to motor and cognitive impairments (Armentano et al. 2007; Tomassy et al. 2010; Alfano et al. 2014; Contesse et al. 2019). In the absence of cortical Nr2f1 in progenitors or early postmitotic neurons, proper barrel fields do not form in the normal S1 region, which seems instead to be respecified into a motor-like cortex (thus named as motorized S1—mS1), as shown by molecular markers and early thalamocortical projections (Armentano et al. 2007; Alfano et al. 2014). Nevertheless, sensory thalamocortical axons are still able to reach the pallial subplate of the affected S1 region in *Nr2f1* cortex-specific mutants, despite its very early acquisition of motor-like molecular identity (Armentano et al. 2007). Interestingly, at postnatal stages, thalamocortical axons fail to functionally innervate the cortical plate, implying that Nr2f1 function within the developing S1 region is necessary for the correct establishment of thalamocortical projections but has little effect on their early arrival. Moreover, the abnormal crosstalk between mS1 and thalamocortical neurons, an important event for the correct development of cortical circuits, suggested that mS1 cells might display multiple functional defects besides the abnormal expression of area-specific molecular markers. To this end, and to understand whether the loss of cortical Nr2f1 leads to a fully functional respecification of sensory to motor identity in mS1, we decided to compare spontaneous activity, as well as intrinsic electrophysiological and morphological properties of mutant mS1 neurons to control (Ctrl) S1 and motor (M1) cortical neurons. More generally, this allowed us to decipher the interactions between identity patterning genes and early activity function during the process of area mapping.

We found that mutant mS1 neurons fail to reproduce intrinsic spontaneous and network activity, as well as morphological and electrophysiological hallmarks, typical of either normal M1 or S1, suggesting a novel role for Nr2f1 in controlling functional specification of S1 properties. Together, our data show that despite imparting a molecular identity of M1-like in S1 cortex, Nr2f1 loss in the cortical primordium results in abnormal spontaneous activity and intrinsic excitability unique to mS1 and different from M1 and S1. This newly described function is accomplished by the transcriptional modulation of several ion channels involved in modulating excitability as well as morphological and structural features of layer V pyramidal neurons (LVPNs).

Materials and Methods

Mice

Nr2f1/COUP-TFI$^{fl/fl}$ mice were crossed with *Emx1-Cre* mice to delete *Nr2f1/COUP-TFI* exclusively in cortical progenitors and their progeny (Armentano et al. 2007). These mice are named *Nr2f1cKO* throughout the text. Mice were genotyped as previously described (Armentano et al. 2007). Control and mutant littermates were *Nr2f1*$^{fl/fl}$ and *Nr2f1*$^{fl/fl}$*:Emx1-Cre*, respectively. For P21 studies, control (*Nr2f1*$^{fl/fl}$) and mutant *Nr2f1cKO* mice were crossed with *Thy1-eYFP-H* mice to specifically label layer V projection neurons (LVPNs), as previously reported (Harb et al. 2016). Midday of the day of the vaginal plug was considered as embryonic day 0.5 (E0.5). Control (*Nr2f1*$^{fl/fl}$) and mutant *Nr2f1cKO* mice were predominantly bred in a C57BL6 background. Both male and female embryos and pups were used in this study. All mouse experiments were conducted according to national and international guidelines, with authorization #15 349 and #15 350 by the French Ministry of Education, Research and Innovation and upon request of the local ethics committee—CIEPAL NCE/2019–548 (Nice) and CEEA50 (Bordeaux), and in accordance with the guidelines established by the Italian National Council on Animal Care and approved by the local Animal Care Committee of University of Turin (Authorization DGSAF 0011710-P-26/07/2017).

MEA Recordings on Primary Cultures and Analysis of MEA Activity

Cortical neuronal cultures were obtained from E18 *Ctrl* and *Nr2f1cKO* mouse fetuses. Somatosensory cortices were rapidly

Downloaded from https://academic.oup.com/cercor/article-abstract/doi/10.1093/cercor/bhaa137/5860958 by University of Canberra user on 25 June 2020

dissected under sterile conditions, kept in cold HBSS (4 °C) with high glucose, and then digested with papain (0.5 mg/ml) dissolved in HBSS plus DNAse (0.1 mg/ml), as previously described (Gavello et al. 2018). Isolated cells were then plated at the final density of 1200 cells/mm^2 onto the MEA (Microelectrode Array, previously coated with poly-DL-lysine and laminin). Cells were incubated with 1% penicillin/streptomycin, 1% glutamax, 2.5% foetal bovine serum, and 2% B-27 supplemented Neurobasal medium in humidified 5% CO_2 atmosphere at 37 °C. Each MEA dish was covered with a fluorinated ethylene-propylene membrane (ALA scientific, Westbury, NY, USA) to reduce medium evaporation and maintain sterility, thus allowing repeated recordings from the same chip.

Multisite extracellular recordings from 59 electrodes were performed using the MEA-system, purchased from Multi-Channel Systems (Reutlingen, Germany). Data acquisition was controlled through MC_Rack software (Multi-Channel Systems Reutlingen, Germany), setting the threshold for spike detection at −30 µV and sampling at 10 kHz. Experiments were performed in a nonhumidified incubator at 37 °C and with 5% CO_2, without replacing the culture medium. Before starting the experiments, cells were allowed to stabilize in the nonhumified incubator for 90 s; then, the spontaneous activity was recorded for 2 min.

Burst analysis was performed using Neuroexplorer software (Nex Technologies, Littleton, MA, USA) after spike sorting operations. A burst consists of high frequency firing of a neuron separated by periods of quiescence (Cotterill et al. 2016); thus, a threshold of at least 3 spikes and a minimum burst duration of 10 ms was set. Algorithm specifications such as maximum interval to start burst (0.17 s) and maximum interval to end burst (0.3 s) were set as in (Gavello et al. 2012; Gavello et al. 2018). Burst analysis was performed by monitoring the following parameters: mean frequency, number of bursts, and mean burst duration. Cross correlation probability values were obtained by means of Neuroexplorer software using ±2-s and 5-ms bin size. All the data collected from active recording sites (i.e., firing activity with spike amplitude >30 µV, i.e., 3× noise value) were pooled by genotype for statistics (N = number of active recording sites, cf., Allio et al. 2015). Detailed number of MEAs recorded per genotype (Ctrl or *Nr2f1cKO*) is provided in Supplementary Table 5.

Ca^{2+} Imaging from *Ex vivo* Brain Slices Preparation and Analysis

Mouse pups at postnatal age (P)1 and P4 were anesthetized on ice, and brains were dissected in ice-cold high-Mg artificial cerebral-spinal fluid (aCSF, containing in mM 125 NaCl, 25 $NaHCO_3$, 2.5 KCl, 7 $MgCl_2$, 2 $CaCl_2$, 1.25 NaH_2PO_4, 10 glucose, and adjusted to pH 7.4) after decapitation. Horizontal 300-µm-thick slices were prepared using a Leica Vibratome 100 M in ice-cold high-Mg aCSF under 95% O_2, 5% CO_2 bubbling. Selected slices were incubated for 1 h at 37 °C in aCSF containing 0.63% Oregon Green BAPTA™ (ThermoFisher O6807 dissolved in DMSO) before proceeding to image acquisition. Slices were loaded on a 35-mm diameter petri dish with 1.3-mm glass bottom and immobilized with a custom nylon net while kept under a constant aCSF perfusion at 37 °C throughout the imaging process. After 30 min of equilibration in the microscope objective holder, time-lapse images were acquired for 15 min at 150-ms intervals using a spinning disk microscope (Olympus/Andor technology) equipped with a 40× air objective. Activity was recorded up to 200 µm below the pia margin.

Images were automatically corrected for drifting using the built-in Fiji function "Linear stack alignment with SIFT" (Schindelin et al. 2012). Single cell borders were manually generated as separate regions of interest (ROIs) using a customized MATLAB script. Each ROI was used to acquire BAPTA fluorescence intensity as the mean of intensity within each ROI area by frame, resulting in a matrix of single cell time series of BAPTA fluorescence signals as a readout of Ca^{2+} cytoplasmic concentration. Matrices were corrected by a moving average (Anderson 1975) normalizing each timepoint with the average of 60 s in each cell and generating a constant baseline over the progressive signal loss due to the bleaching of the BAPTA dye. As a cutoff for detecting cells actively displaying Ca^{2+} transients, we discarded from the analysis those cells whose first quartile of intensity did not contain at least 40% of its timepoints, since cells below this threshold showed values comparable to noise signals. For each experiment, we measured the ratio of active and inactive cells (see also Supplementary Fig. 2; Supplementary Table 1). For the remaining selected timeseries, Ca^{2+} transients were detected filtering BAPTA intensity on a threshold of 3 SD. The bursting frequency of every selected cell was measured by dividing the number of transients above threshold by the sum of intervals between each burst. To evaluate activity coordination, we counted the ratio of transients occurring across cells in a sliding window interval of 3 s normalized by the total number of transients. All time-lapse analyses were performed using a custom MATLAB script.

Ex vivo Whole-Cell Electrophysiology and Analysis

P5 to P8 pups were decapitated, and brains were placed on ice-cold modified artificial cerebrospinal fluid (aCSF) containing (in mM): 87 NaCl, 25 $NaHCO_3$, 5 Glucose, 65 Sucrose, 2.5 KCl, 1.25 NaH_2PO_4, 0.5 $CaCl_2$, and 7 $MgCl_2$ saturated with 95% CO_2 and 5% O_2. Coronal slices of 300-µm thickness were cut using a vibratome (Vibratome 300 Plus, Sectioning Systems) and gently transferred to room temperature aCSF containing (in mM): 125 NaCl, 25 $NaHCO_3$, 25 Glucose, 2.5 KCl, 1.25 NaH_2PO_4, 2 $CaCl_2$, and 1 $MgCl_2$ saturated with 95% CO_2 and 5% O_2 (pH 7.4). Current-clamp recordings were performed at 32–34 °C using a potassium gluconate-based intracellular solution containing (in mM): 120 K-Gluconate, 20 HEPES, 0.5 EGTA, 15 KCl, 4 MgATP, and 0.3 NaGTP (pH 7.4) and osmolarity set to 299 mosmol/l. Biocytin (1.5–2 mg/ml) was added to the intracellular solution for *post hoc* immunohistochemistry. Neurons were visualized with an upright microscope (Zeiss Axio Examiner D1) equipped with an Evolve 512 EMCCD Camera (Photometrics) using a 63X/1.0 nA water-immersion objective (Zeiss) and infrared DodT contrast imaging. Recording pipettes (6–10 MΩ) were pulled from borosilicate glass using a Narishige P-10 puller. Data were acquired using a Dagan BVC-700A Amplifier, low-pass filtered at 3 kHz, and sampled at 20 kHz with ITC16 (Instrutech) and AxoGraph X software. Membrane voltage was recorded in the bridge mode. To determine the excitability of pyramidal neurons, 800-ms square current steps of 10 pA from −100 to +150 pA were set.. The rheobase was defined as the minimum somatic current required to elicit an action potential (AP) from the resting membrane potential (V_{rest}) of the neuron. Input resistance (R_{in}) was calculated from voltage responses to −20 pA. Threshold potential was defined as $dV/dt = 10$ mV/ms. Interspike interval (ISI) was calculated as the difference between first and second AP at the minimal current to elicit >2AP. The amplitude of APs was measured from spike threshold (see Supplementary Table 2). AP

Downloaded from https://academic.oup.com/cercor/article-abstract/doi/10.1093/cercor/bhaa137/5860958 by University of Canberra user on 25 June 2020

width was measured at half of the maximum amplitude (APhalf-width or AP*h-w*). Voltage sag was calculated as the difference between negative voltage peak and steady-state hyperpolarization from traces in which the difference between steady-state response and baseline fell within 20–30 mV. Firing frequency was calculated by dividing the number of APs by the duration of the current step (800 ms). Membrane time constant (τ_m) was calculated as the slow component of a double exponential fit of the decay (recovery) from the average of 10 hyperpolarizing current pulses (1 ms 400 pA). Capacitance was obtained as the ratio of membrane time constant over R_{in}.

Post Hoc Immunofluorescence

Brain slices were fixed overnight (ON) at 4 °C with 4% paraformaldehyde in 0.1 M phosphate buffer (PB) pH 7.4. The following day slices were washed 3 × 10 min with 0.1 M PB and incubated overnight (ON) at 4 °C with Alexa-Fluor®-conjugated streptavidin diluted 1:500 in 0.1 M PB. The day after, slices were washed 3 × 10 min with 0.1 M PB, stained with DAPI, and finally mounted with Mowiol.

KCl *Ex Vivo* Depolarization Assay

Ctrl and *Nr2f1cKO* P7 pups were sacrificed by decapitation and brains dissected into ice-cold aCSF saturated with 95% O_2 and 5% CO_2. 300 µm-thick slices were produced by vibratome sectioning and then transferred into room temperature aCSF, and constantly saturated with 95% O_2 and 5% CO_2. After 15 min of acclimatization, slices from both genotypes were split into two groups: an untreated group (**−KCl**) and an experimental group (**+KCl**). KCl was added at the final concentration of 7 mM to the aCSF of the experimental group, whereas control slices were kept in normal aCSF. After an incubation time of 6 h (Dumitrescu et al. 2016), slices were washed for 15 min in newly prepared aCSF and then processed for immunofluorescence (IF), as described below.

Histology and Immunohistochemistry of Mouse Perinatal Cortices

P7 to P8 pups were anesthetized by using a mixture of Tiletamine-Zolazepam-Xylazine-Buprenorphine (TZXB) and intracardially perfused with PB Saline (PBS) followed by 4% paraformaldehyde (PFA) in PBS. Then, brains were dissected and postfixed for 4 h at 4 °C in 4% PFA and then vibratome-sectioned to obtain 100-µm thick, coronal, or sagittal floating sections. ON incubation at 4 °C in a solution of 0.5% Triton X-100, 3% BSA, 10% goat serum in PBS was performed to permeabilize the sections and reduce nonspecific binding of the antibodies. For IF, sections were incubated for 2 days at 4 °C with indicated primary antibodies in a solution of 0.5% Triton X-100, 10% goat serum in PBS, and then ON at 4 °C with relative secondary antibodies and HOECHST diluted in PBS. For the complete list of primary and secondary antibodies, see Supplementary Table 4C. For HCN1 IF, brains were briefly postfixed for 30 min at 4 °C in 4% PFA and then immediately sectioned with the vibratome to obtain 50-µm-thick, coronal floating sections. Permeabilization-blocking step was reduced to 2 h, primary antibody incubation to one ON and secondary antibody and HOECHST incubation to 2 h. Sections were then transferred on superfrost plus slides (ThermoScientific), let dry for 30 min to 1 h, and finally mounted with Mowiol mounting medium.

Microscopy and Image Analysis

Imaging was performed using a Zeiss 710 confocal microscope equipped with a 405-nm diode, an argon ion, a 561-nm DPSS, and a 647 HeNe lasers. Z-stacks of fixed cortical sections were imaged using a LD-LCI Plan-Apo 25x/0.8 NA or a LD Plan-Apo 63x/1.4 NA oil immersion lenses. Images from IF experiments were analyzed by using Fiji-ImageJ Software (Schindelin et al. 2012): cell counter plug-in was used to assess the number of cells expressing specific proteins, while measurement tools were used to determine signal intensity or axonal initial segment (AIS) features such as length and distance from the soma. For the AIS average diameter measurement, we took advantage of the IMARIS software tool filament tracer (Oxford Instruments). AISs were semi-automatically reconstructed, and an average diameter automatically measured for every AIS individually.

Morphological characterization of biocytin filled LVPNs was analyzed using IMARIS. Cell arborization was reconstructed in a semi-automatic manner, *via* the filament tracer module. Automatic length measuring tool was used to calculate the total and basal dendritic length. Branching points, branching point orders, and tips were manually quantified for both basal and apical dendrites, as well as primary and lateral dendrites. The branch tip order is an integer value equivalent to the number of branching points; a dendrite undergoes from its somatic origin to the terminal tip (see also Fig. 4E for a graphic representation). Primary dendrites were identified as directly originating from the soma; lateral dendrites were categorized as originating from and perpendicular to the apical dendrite, whereas total and basal branch tips were identified as the terminal ends of primary dendrites including or excluding the apical dendrite arborization, respectively.

The basal Dendritic Complexity Index (bDCI) was calculated as [($\sum$ Basal branch tip orders + Basal branch tips)/Primary dendrites] × Basal Arbor Length.

An automatic detection of Sholl intersections was used to compute Sholl profiles for every individual cell. Sholl intersections were identified as the number of dendrite intersections for concentric spheres of increasing radius (10-µm difference) and having as a center the centroid of the cell body (see also Supplementary Table 3).

RNA Extraction and cDNA Synthesis

RNA for reverse transcriptase–PCRs (RT–PCRs) was extracted from P7 dissected neocortices separated from meninges of *Ctrl* and *Nr2f1cKO* mice ($n = 3$) using the RNeasy Mini kit (Qiagen) following manufacturer's instructions. RNA quantity and RNA quality were assessed with Nanodrop and gel electrophoresis. cDNA was synthetized from 1 µg of total RNA using Superscript III First-Strand Synthesis System for RT–PCR (Invitrogen) following manufacturer's instructions.

qPCR RNA/cDNA Quantification

Quantitative polymerase chain reaction (qPCR) on cDNA was performed using KAPA Sybr Fast (Kapa Biosystems) according to manufacturer's instructions. Samples were run on a LigthCycler II 480 (Roche) with the primers listed in Supplementary Table 4A. Each reaction consisted of 10ng total cDNA, with 200 nM forward-reverse primer mix. Amplification take-off values were evaluated using the built-in LightCycler relative quantification analysis function, and relative expression was calculated with

Downloaded from https://academic.oup.com/cercor/article-abstract/doi/10.1093/cercor/bhaa137/5860958 by University of Canberra user on 25 June 2020

the $2^{-\Delta\Delta Ct}$ method. Gene expression was normalized to the housekeeping gene GAPDH.

Dissection and Western Blot of Mouse Perinatal Cortices

P7-P8 pups were sacrificed by decapitation, and fresh tissues were dissected immediately after. Whole cortex samples were collected and lysed in RIPA buffer [10 mM Tris-Cl (pH 8.0), 1 mM EDTA, 1% Triton X-100, 0.1% sodium Deoxycholate, 0.1% SDS, 140 mM NaCl, 1 mM PMSF] implemented with Complete protease inhibitors (Roche). Protein quantity was then measured with the Pierce BCA protein assay KIT (ThermoScientific). Equal amounts of proteins from tissue lysates were resolved by reducing SDS-PAGE, transferred to PolyVinylidene DiFluoride membrane, and incubated with the indicated antibodies (see Supplementary Table 4C). Immunoblots were developed using ECL prime western blotting detection reagent (GE Healthcare). Signals were normalized to actin signal intensity.

Chromatin Immuno-Precipitation (ChIP)

The ChIP protocol was modified from Alfano et al. (2011) using protein Sepharose-A resin (SIGMA), prepared by washing in PBS and equilibration buffer (HEPES pH 7.4 20 mM, EDTA 1 mM, NaCl 150 mM, Triton 0.8%, SDS 0.1% PMSF 10 mg/ml). For each experiment ($n = 3$), cortices from 8 mice at P0 were collected in ice-cold HBSS and washed in DMEM. Samples were crosslinked in 0.9 formaldehyde for 10 min and blocked adding 1.1 mL of glycine 1.25 M for 5 min. Samples were rinsed in washing buffer (HEPES pH 7.4 20 mM, NaCl 150 mM, Glycine 0.125 M, PMSF 10 mg/ml). Nuclei were extracted in lysis buffer (HEPES pH 7.4 20 mM, NaCl 150 mM, Glycine 0.125 M, SDS 1% PMSF 10 mg/ml) and collected by centrifugation (2200rcf for 5 min) before sonication in 1.2-mL sonication buffer (HEPES pH 7.4 20 mM, NaCl 150 mM, Glycine 0.125 M, SDS 0.4% PMSF 10 mg/ml) six times for 5 s. DNA fragments were separated from cellular debris by spinning at 14000rcf for 10 min. After collecting the supernatant, fragmentation quality was evaluated by gel electrophoresis. DNA fragments were split in 3×300 µl samples and precleared with resin Slurry solution (resin/equilibration buffer, 50/50 volume) by adding 50 µL of this solution to each sample and incubating for 1 h at 4 °C. Supernatant was collected after spinning at 800rcf for 2 min at 4 °C and incubated ON at 4 °C with 3 µg of dedicated antibodies: Nr2f1 antibody (Thermo Fisher PA5–21611) and GFP antibody (Abcam ab13970, as an internal negative control for aspecific binding). A sample called Mock was obtained using a blank volume of Sonication buffer with no antibody. About 50 µL of Slurry solution was added to each sample, and all samples were incubated 3 h at 4 °C and washed four times in ice-cold washing buffer A (HEPES pH 7.4 20 mM, NaCl 150 mM, Triton 100 1%, SDS 0.1% PMSF 10 mg/ml), four times in ice-cold washing buffer B (Tris pH 8.0 20 mM, EDTA 1 mM, LiCl 250 mM, NP-40 0.5%, Na-Deoxycholate 0.5%, PMSF 10 mg/ml), and two times in TE buffer (Tris HCl pH 8.0 20 mM, EDTA 1 mM, PMSF 10 mg/ml). Finally, DNA fragments were eluted by adding 300 µL of Elution buffer (NaHCO3 50 mM, 1% SDS) and incubating in rotation 1 h at RT. Input samples were generated by mixing 300 µL of elution buffer to 10 µL of the supernatant from the first washing of a sample without antibody. Fragments were separated from the resin and antibodies by spinning twice at 8000rcf for 2 min and recovering the supernatant. Next, we reversed crosslink by adding 12 µL of NaCl 5 M to the samples and by incubating ON at 65 °C. Any RNA contamination was removed by adding 1 µL of RNAse-A 10 mg/ml and incubating for 30 min at 37 °C; the reaction was blocked adding 6 µL of EDTA 0.5 M. Remaining proteins were digested by adding 12 µL of Tris HCl pH 8.0 and 1 µL of proteinase K 10 mg/ml for 1–2 h at 45 °C. Finally, samples were purified by phenol-chloroform extraction and precipitated into 20 µL of H_2Omq.

qPCR of ChIP Samples

qPCRs on ChIP were performed using KAPA Sybr Fast (Kapa Biosystems) according to manufacturer's instructions. Samples were run on a LigthCycler II 480 (Roche) with the primers listed in Supplementary Table 4B. For each reaction of 0.5 µL of sample, 0.2 µM of primers were added. For proper quantification, a calibration curve was calculated, by running six sequential 1:10 dilutions of a sample with known starting concentration for each set of primers. Each reaction was carried out in three technical replicates: negative controls including the use of aspecific antibody, no antibody, and mock and input samples. Samples were normalized on the input and set to 1, and the fold change was then calculated as the ratio between specific antibodies samples to aspecific antibody controls.

Statistical Tests

Hierarchical clustering was performed with Euclidean distance, using both average burst frequency and correlation per condition. In Figure 2, three-way ANOVA to determine relevant parameters driving differences for Ca^{2+} transient frequency, coordination, and frequency variability was used; *post hoc* testing was performed using Welch two-samples test. In Figure 6A, Welch's unequal variances *t*-test analysis correcting the *P*-value for multiple testing using the Benjamini–Hochberg procedure, false discovery rate = 0.25 was utilized. Data analysis scripts were custom-prepared in R (Computing RFfS 2018) and MATLAB. Additional statistical analyses were also performed using Graphpad Prism7, and data are presented as mean ± SEM. *n* values represent biological replicates from ≥3 different brains and ≥3 different litters as stated in each figure legends or supplementary tables. No statistical tests were used to predetermine sample size, but samples sizes were similar as reported in previous publications (Del Pino et al. 2013; Del Pino et al. 2017) or as generally employed in the field. No randomization was used. Whenever possible, both genotypes were processed in parallel on the same day. *Ex vivo* electrophysiology experiments and analysis of all data were performed before genotyping. Differences were considered significant when $P < 0.05$. Data sets were tested for normality (Kolmogorov–Smirnov) or homoscedasticity (Levene test) before performing parametric (Student *t*-test, one-way, two-way, or three-way ANOVA followed by Bonferroni's *post hoc* test) or nonparametric tests (Welch's unequal variances *t*-test or Mann–Whitney test) used to determine *P*-values (See also Supplementary Tables 1–5).

Results

Altered Intrinsic Network and Bursting Activity in Cultured *Nr2f1*-Deficient Cortical Neurons

To understand whether early molecular misspecification of mS1 was accompanied by changes in intrinsic neocortical activity, we first assessed network activity in neocortices lacking *Nr2f1* independently of thalamic afferents by employing a conditional mutant mouse in which *Nr2f1* is exclusively deleted from the cortex (referred as *Nr2f1cKO*). We compared

Downloaded from https://academic.oup.com/cercor/article-abstract/doi/10.1093/cercor/bhaa137/5860958 by University of Canberra user on 25 June 2020

network activity of dissociated mutant mS1 cortical neurons to that of *Ctrl* M1 and S1 neurons at E18.5 by culturing them onto microelectrode arrays (MEAs). This allowed us to follow activity in an *in vitro* embryo-derived model at different times of cortical network maturation in the absence of subcortical inputs and assess the possible effect of cell-autonomous developmental programs on functional network organization (Fig. 1 and Supplementary Fig. 1).

Our recordings of primary-cultured neuronal networks started at 9DIV, since 6DIV neuronal cultures failed to show any activity in either *Ctrl* or *Nr2f1cKO* conditions. A comparison of the average firing frequency of the earliest events taking place at 9DIV showed a significantly lower firing frequency in mS1 *Nr2f1cKO* than in *Ctrl* S1 and M1 networks (Fig. 1A–D). In addition, whereas there was no significant difference in the average number of bursts recorded from *Ctrl* S1 and *Nr2f1cKO* mS1 networks, both of them displayed significantly lower burst numbers when compared to *Ctrl* M1 networks (Fig. 1E). We also found that the burst duration of *Ctrl* M1 and mutant mS1 was higher than that of *Ctrl* S1 neurons (Fig. 1F). However, firing activity was more organized into bursts in *Nr2f1cKO* mS1 neurons than in *Ctrl* S1 and M1, resulting in a higher firing synchronization index (Fig. 1G–H). These findings show that at 9DIV, loss of *Nr2f1* leads to an overall reduced firing frequency but prolonged burst duration and increased network synchronization in mS1 neurons when compared to control M1 and S1.

To explore the maturation of this cortical network activity, we performed similar experiments in neuronal cultures at 15DIV and 20DIV (Supplementary Fig. 1). At 15DIV, we observed that the firing frequency of *Ctrl* cortical networks reached a higher value than at 9DIV and 20DIV (data not shown). We therefore compared firing parameters measured at 15DIV with those measured at 9DIV to assess whether network maturation was affected *in vitro*. Interestingly, the extent of developmental increase in firing activity, number of bursts, and burst duration was lower in *Nr2f1cKO* mS1 and *Ctrl* M1 neuronal networks than in *Ctrl* S1 (Supplementary Fig. 1A–C). Since network maturation correlates with the expression of synchronized events organized in bursts, the evaluation of the percentage of spikes organized in bursts and the cross correlation index represent two parameters of network maturation *in vitro* (Gavello et al. 2012; Gavello et al. 2018). We found that the percentage of spikes within bursts (Supplementary Fig. 1D), as well as the cross-correlation index (Supplementary Fig. 1E), were significantly smaller in both *Nr2f1cKO* mS1 and *Ctrl* M1 neurons compared to *Ctrl* S1 neurons. These data unveil that network properties, involved during maturation of *Ctrl* M1 neurons, are similar in *Nr2f1cKO* mS1 but not in *Ctrl* S1 neurons.

Finally, the differences in firing patterns here reported are determined by a combination of neuronal intrinsic and synaptic factors, such as network connectivity, potentially related to glial function. Despite glial cells being fundamental for neuronal function and network maturation, we have not specifically investigated potential changes in glial cell number or function in *Nr2f1cKO* mS1-derived cultures, and rather focused our investigation on neuronal factors.

Alterations in Ca2$^+$ Transients and Synchronous Activity in Early Postnatal *Nr2f1*-Deficient Cortices

As a further step toward understanding how spontaneous cortical network activity develops in the immature *Nr2f1cKO* mouse pups, we set up a Ca^{2+} imaging protocol in *ex vivo* acute brain slices of P1 and P4 mouse pups using the calcium indicator Oregon Green BAPTATM (TM superscript please). These two stages represent critical timepoints of early cortical somatosensory circuit establishment bridging the activity from spontaneous thalamic waves (Anton-Bolanos et al. 2019) to experience-driven thalamic inputs (Corlew et al. 2004). Cells that displayed Ca^{2+} transients as a result of prolonged neuronal activation typical of excitatory neurons were recorded over 15 min (Fig. 2, see Materials and Methods). To evaluate the level of cortical network maturation, we measured the correlation index of Ca^{2+} transients for each experiment. This index is a measure of simultaneously active cells during a specific transient and is calculated as the ratio of active neurons displaying a Ca^{2+} transient within a 3-s window, normalized on the total number of active neurons and the total amount of transients within the same experiment (Fig. 2A and Supplementary Fig. 2, see Materials and Methods).

At P1, we observed differences in Ca^{2+} transient frequency (Hz) between *Ctrl* M1 and S1 and between *Ctrls* and *N2rf1cKO* mS1, indicating that the mS1 network retains properties distinct from both S1 and M1 (Fig. 2B and Supplementary Table 1). At P1, the Ca^{2+} correlation index did not display differences across either areas or genotypes (Fig. 2C and Supplementary Table 1), implying that no evident circuit maturation differences were found at this stage. At P4, an overall increase of Ca^{2+} transient frequency (Hz) was observed in all conditions (Fig. 2B and Supplementary Table 1), in line with previous observations (Corlew et al. 2004). At this stage however, comparison of the correlation index among areas and genotypes showed a statistical difference between *Ctrl* M1 and S1 as well as between *Ctrl* S1 and *Nr2f1cKO* mS1 (Fig. 2C and Supplementary Table 1). This was accompanied by an overall decrease of the variability of Ca^{2+} transient frequency in *Ctrl* S1 and M1, indicating higher coherence of spontaneous activity across measured cells (Fig. 2D and Supplementary Table 1). On the other hand, *N2rf1cKO* mS1 cells failed to show any significant decrease of the variability of Ca^{2+} transient frequency (Fig. 2D and Supplementary Table 1).

Taken together, our data show that loss of Nr2f1 function alters Ca^{2+} frequency and Ca^{2+} correlation index of mutant mS1 cells at perinatal stages.

Abnormal Intrinsic Electrophysiological Properties in Early Postnatal *Nr2f1*-Deficient Cortical LVPNs

Since intrinsic electrophysiological properties are related to the expression of neural activity, we next examined the state of the intrinsic excitability of pyramidal neurons in *Nr2f1cKO* mouse cortices, previously shown to express an altered molecular signature (Tomassy et al. 2010; Harb et al. 2016). We measured their intrinsic excitability profile in *Ctrl* M1 and S1 as well as *Nr2f1cKO* mS1 in acute brain slices from 5- to 8-day old (P5–8) mouse pups. At this developmental stage, corticogenesis and neural migration already took place, and neocortical neurons have differentiated from an immature spiking phenotype, acquiring instead a regular type of spiking (Massengill et al. 1997). We employed whole-cell recordings in current-clamp mode and performed the measurements in the absence of synaptic blockers since, at this developmental stage, the number of synaptic inputs is very low (Favuzzi et al. 2019) and spontaneous activity rarely occurred in our recording conditions. In order to compare electrophysiological properties of *Ctrl* M1 and S1 with those of

Downloaded from https://academic.oup.com/cercor/article-abstract/doi/10.1093/cercor/bhaa137/5860958 by University of Canberra user on 25 June 2020

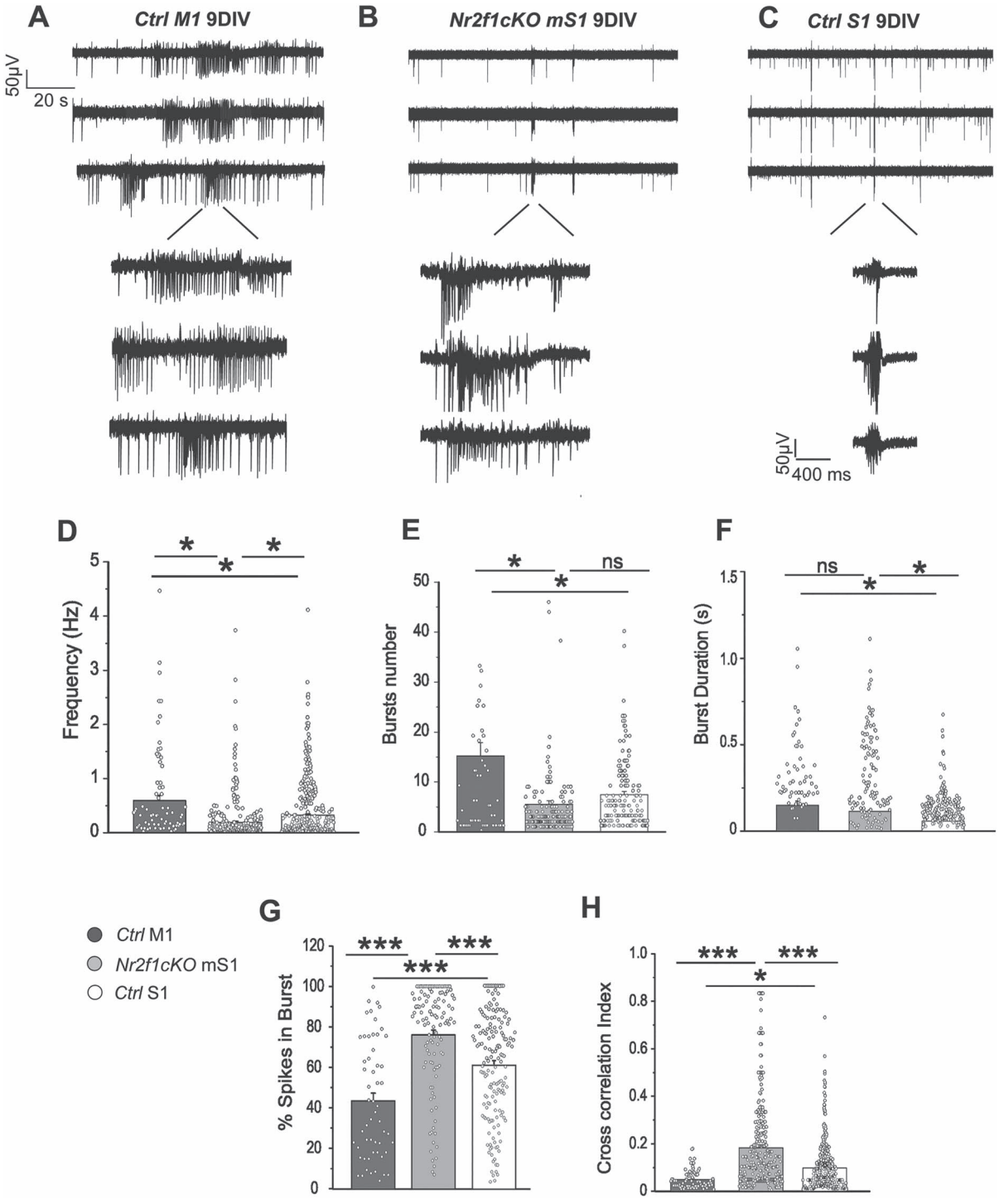

Figure 1. Impaired intrinsic network and bursting activity recorded in DIV 9 cultured *Nr2f1*-deficient cortical neurons. (*A–C*) Spontaneous firing of *Ctrl* S1, *Nr2f1cKO* mS1, and *Ctrl* M1 cortical network recorded by three representative MEA at 9DIV. In insets, representative bursts shown at expanded scale. Firing parameters from *Ctrl* S1 ($N = 10$), *Nr2f1cKO* mS1 ($N = 12$), and *Ctrl* M1 ($N = 7$) MEAs are compared. (*D*) Average firing frequency from *Ctrl* M1 MEA was 0.63 ± 0.16 Hz ($N_{channels} = 76$), from *Nr2f1cKO* mS1 MEA was 0.30 ± 0.04 Hz ($N_{channels} = 208$), and from *Ctrl* S1 MEA 0.41 ± 0.04 Hz ($N_{channels} = 271$). (*E*) Average bursts number from *Ctrl* M1 MEA was 14.91 ± 2.73 ($N_{channels} = 56$), from *Nr2f1cKO* mS1 MEA was 5.51 ± 2.73 ($N_{channels} = 203$), and from *Ctrl* S1 MEA was 7.21 ± 0.67 ($N_{channels} = 170$). (*F*) Average burst duration from *Ctrl* M1 MEA was 0.38 ± 0.07 s ($N_{channels} = 56$), from *Nr2f1cKO* mS1 MEA was 0.31 ± 0.02 s ($N_{channels} = 112$), and from *Ctrl* S1 MEA 0.15 ± 0.02 s ($N_{channels} = 169$). (*G*) Percentage of spikes in burst from *Ctrl* M1 MEA was $43.08 \pm 3.88\%$ ($N_{channels} = 56$), from *Nr2f1cKO* mS1 was $76.03 \pm 2.39\%$ ($N_{channels} = 114$), and from *Ctrl* S1 MEA was $60.96 \pm 2.06\%$ ($N_{channels} = 167$). (*H*) Cross correlation index from *Ctrl* M1 MEA was 0.05 ± 0.01($N_{channels} = 56$), from *Nr2f1cKO* mS1 MEA was 0.18 ± 0.01 ($N_{channels} = 258$), and from *Ctrl* S1 MEA was 0.09 ± 0.01 ($N_{channels} = 256$). Data are represented as mean ± SEM. Significativity is shown above: $^*P < 0.05$; $^{**}P < 0.01$, $^{***}P < 0.001$. ns, not significant. Sampling and statistical test listed in Supplementary Table 5.

Downloaded from https://academic.oup.com/cercor/article-abstract/doi/10.1093/cercor/bhaa137/5860958 by University of Canberra user on 25 June 2020

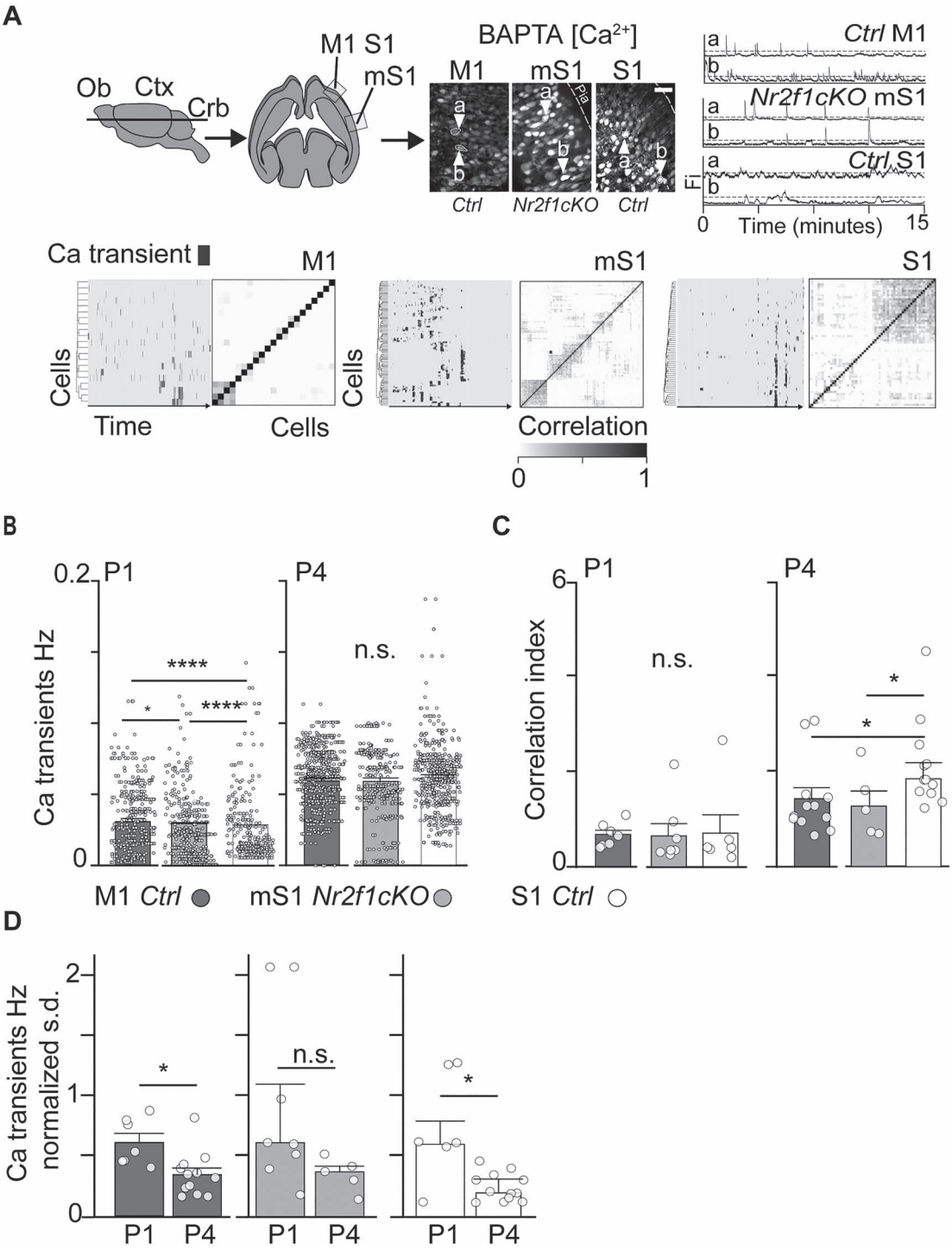

Figure 2. Altered Ca^{2+}-dependent intrinsic activity upon *Nr2f1* loss. (*A*) Top left: schematics of the acute horizontal slice preparation, from which we recorded the primary motor (M1) and somatosensory (S1) areas (S1 and M1 in *Ctrl* and mS1 in *Nr2f1cKO brains*) based on their respective rostral and medial position. Top center: representative image of the Ca^{2+} BAPTA fluorescent signals for each area. Top right: time series of intracellular signals in manually defined cells (indicated in the previous panels with white arrowheads) corrected by moving average (Fi). Ca^{2+} transients are defined by distinct thresholds. Bottom: time series matrices of above threshold Ca^{2+}. Single traces have been sorted by Euclidean distance (left). Pearson correlation matrices of single neuron signal traces within single experiment (right). Distribution of single cell Ca^{2+} transient frequency (Hz) (*B*) and transient intraneuron correlation (*C*) in P1 and P4 brains. For Ca^{2+} transients, single points indicate cells; for Ca^{2+} correlation, single points are single time-lapse images; some slices have been recorded multiple times; each animal was recorded over more slices. (*D*) Standard deviation (s.d.) of Ca^{2+} transients frequency normalized to the mean indicates a progressive decrease of frequency variability with age in both *Ctrl* M1 and S1, while no decrease is measured in *Nr2f1cKO* mS1. Statistical scripts were custom-prepared in R (Computing RFfS 2018). Sampling and statistical tests are listed in Supplementary Table 5. Abbreviations: Ob, Olfactory bulb; Ctx, Cortex; Crb, Cerebellum; M1, motor cortex; mS1, motorized somatosensory cortex; P, postnatal day; and S1, somatosensory cortex. $^{*}P < 0.05$, $^{**}P < 0.01$, $^{****}P < 0.001$. Scale bar: 10 µm. See also Supplementary Figure 2 and Supplementary Tables 1 and 5.

Downloaded from https://academic.oup.com/cercor/article-abstract/doi/10.1093/cercor/bhaa137/5860958 by University of Canberra user on 25 June 2020

Nr2f1cKO mS1 neurons, we focused on similar neuronal populations by selecting neurons that were identified as layer V pyramidal neurons (LVPNs), as defined by *post hoc* morphological reconstructions. Although LVPNs differentiate into two major types in terms of morphology and intrinsic physiology in adult brains, these two LVPN types are not well differentiated at the electrophysiological level during early postnatal stages (Kasper et al. 1994; Christophe et al. 2005). Among all recorded cells, we analyzed 28 *Nr2f1cKO* neurons in mS1 (from 7 different brains) as well as 10 *Ctrl* M1 and 19 *Ctrl* S1 neurons (from 8 different brains) located within the layer V and displaying a slowly adapting regular spiking firing pattern (Fig. 3A). Notably, specific changes in passive and active electrophysiological properties were observed in *Nr2f1cKO* mS1 neurons when compared to both *Ctrl* M1 and S1 neurons (Supplementary Table 2). Mutant mS1 LVPNs displayed a more depolarized resting membrane potential (V_{rest}) than *Ctrl* S1 LVPNs, but no significant differences when compared to *Ctrl* M1 LVPNs (Fig. 3B). In addition, mS1 LVPNs displayed a significantly decreased rheobase compared to *Ctrl* M1 and S1 LVPNs (Fig. 3C). Interestingly, *Nr2f1cKO* mS1 LVPNs also exhibited a reduced voltage sag in response to hyperpolarizing current steps, suggesting a more reduced I_h than *Ctrl* LVPNs (Fig. 3D). Finally, *Nr2f1cKO* mS1 LVPNs also exhibited a significantly higher maximum firing frequency than *Ctrl* M1 LVPNs, but no significant differences when compared to *Ctrl* S1 LVPNs (Supplementary Table 2). No significant changes in input resistance, AP threshold, AP amplitude, AP half-width, ISI, latency for AP generation, membrane time constant (τ_m), or capacitance were observed in mutant LVPNs (Supplementary Fig. 3 and Supplementary Table 2). Taken together, this functional characterization suggests that within the immature and *Nr2f1*-deficienct mS1 cortex, LVPNs display alterations in their intrinsic excitability. Particularly, these neurons show a unique electrophysiological signature differing from *Ctrl* S1 and M1 LVPNs in some but not all intrinsic properties.

Reduced Dendritic Complexity of LVPNs in *Nr2f1* Mutant Cortices

To assess whether abnormal intrinsic excitability of P5-P8 mutant mS1 LVPNs was accompanied by changes in dendritic morphology, we reconstructed and analyzed the LVPNs that were filled with biocytin after patch clamp recording (Fig. 4A–C). We first evaluated dendritic arbor geometry and complexity by performing Sholl analysis. Comparison of Sholl profiles revealed that mS1 *Nr2f1cKO* LVPNs had a significantly reduced proximal dendritic branching pattern (20–100 µm from the soma) than both *Ctrl* M1 and S1 LVPNs (Fig. 4D and Supplementary Table 3), whereas minor or no differences were observed in distal regions (Supplementary Fig. 4A and Supplementary Table 3). Next, to evaluate more specific features of the dendrite geometry, we assessed the basal dendrite complexity index (bDCI), arbor length, number of primary dendrites, branching points and tips, and oblique formations of basal and apical dendrites of mutant mS1 and *Ctrl* M1 and S1 neurons (Fig. 4E–I and Supplementary Fig. 4B–D). Our morphological data point to a generally less elaborate basal dendrite formation in mutant mS1 LVPNs, whereas no significant differences were observed in apical and oblique dendrite geometry between *Nr2f1cKO* mS1 neurons and *Ctrl* M1 and S1 neurons. In particular, the bDCI was significantly reduced in *Nr2f1cKO* mS1 LVPNs compared to *Ctrl* cells from M1 and S1 cortices (Fig. 4E–F), as a result of a reduced number of primary dendrites, branching points, and terminal tips (Fig. 4G–I). Overall, our data indicate that the loss of Nr2f1 function affects the complexity of LVPN basal dendrite geometry in mS1 at early postnatal stages. Moreover, the structural differences observed between *Ctrl* M1 and mutant mS1 LVPNs show that despite expressing CTIP2, a bona fide marker for LVPNs (Armentano et al. 2007; Tomassy et al. 2010), these neurons differ in their morphological complexity and electrophysiological properties.

Reduced Conformation and Plasticity Properties of the Axon Initial Segment in Mutant *Nr2f1* LVPNs

Intrinsic excitability and dendritic changes are often associated with variations in the structural properties of the axon initial segment (AIS), a specialized structure playing a pivotal role in the integration of synaptic inputs and AP initiation (Kole and Stuart 2012; Yamada and Kuba 2016). It has been reported that distinct AIS features, such as length and/or location relative to the soma, are crucial for the homeostatic control of neuronal excitability in LVPNs (Hamada et al. 2016). The observed reduction of basal dendrite complexity, sag response, and the presence of a more depolarized resting membrane potential in mS1 (Fig. 3 and Supplementary Fig. 3) led us to hypothesize that structural changes of the AIS could occur in *Nr2f1cKO* LVPNs. This could act as a potential mechanism stabilizing AP generation, as observed in previous studies (Gulledge and Bravo 2016; Hamada et al. 2016). To test this hypothesis, we analyzed the AIS structure of P7 LVPNs *Ctrl* S1 and *Nr2f1cKO* mS1 cortices employing the cytoskeletal scaffolding protein Ankyrin G —a widely used marker of the AIS— (Kordeli et al. 1995; Zhou et al. 1998), together with CTIP2 (Arlotta et al. 2005), and NeuN, a neuronal marker labeling the soma (Fig. 5). Notably, we found a significantly reduced length and diameter of the Ankyrin-positive AIS as well as decreased distance from the soma in *Nr2f1cKO* mS1 compared with *Ctrl* S1 LVPNs (Fig. 5A–D). This suggests that altered intrinsic excitability and dendritic structure of mutant LVPNs might be correlated with changes in AIS conformation and localization (Grubb and Burrone 2010; Kuba 2010; Kuba et al. 2010; Wefelmeyer et al. 2016). Decreased length and diameter were also observed in P21 LVPNs (Fig. 5E–G), suggesting that altered AIS structure observed at P7 is most probably not the result of delayed neuronal maturation.

Finally, to assess whether the AIS of *Nr2f1*-deficient LVPNs would still respond to a plasticity-inducing stimulus despite its already reduced length and diameter, we applied a chronic depolarization protocol to *Ctrl* and *Nr2f1cKO* P7 acute brain slices (see Materials and Methods). In agreement with previous studies (Dumitrescu et al. 2016), the depolarization treatment reduced the relative AIS length of *Ctrl* LVPNs. In contrast, no significant changes were observed in the AIS size between depolarization and control treatment of *Nr2f1*-deficient LVPNs (Supplementary Fig. 5A,B). The failure of AIS response to increased neuronal activity in *Nr2f1*-deficient LVPNs suggests a common mechanism between increased excitability and loss of *Nr2f1* function.

Altered Expression of Ion Channels and Glutamate Receptors in Postnatal Cortices of *Nr2f1cKO* Mutants

Since neuronal intrinsic excitability is primarily determined by the expression, subcellular distribution, and biophysical properties of ion channels, we next tested the hypothesis that loss of *Nr2f1* function might alter neuron properties and

Downloaded from https://academic.oup.com/cercor/article-abstract/doi/10.1093/cercor/bhaa137/5860958 by University of Canberra user on 25 June 2020

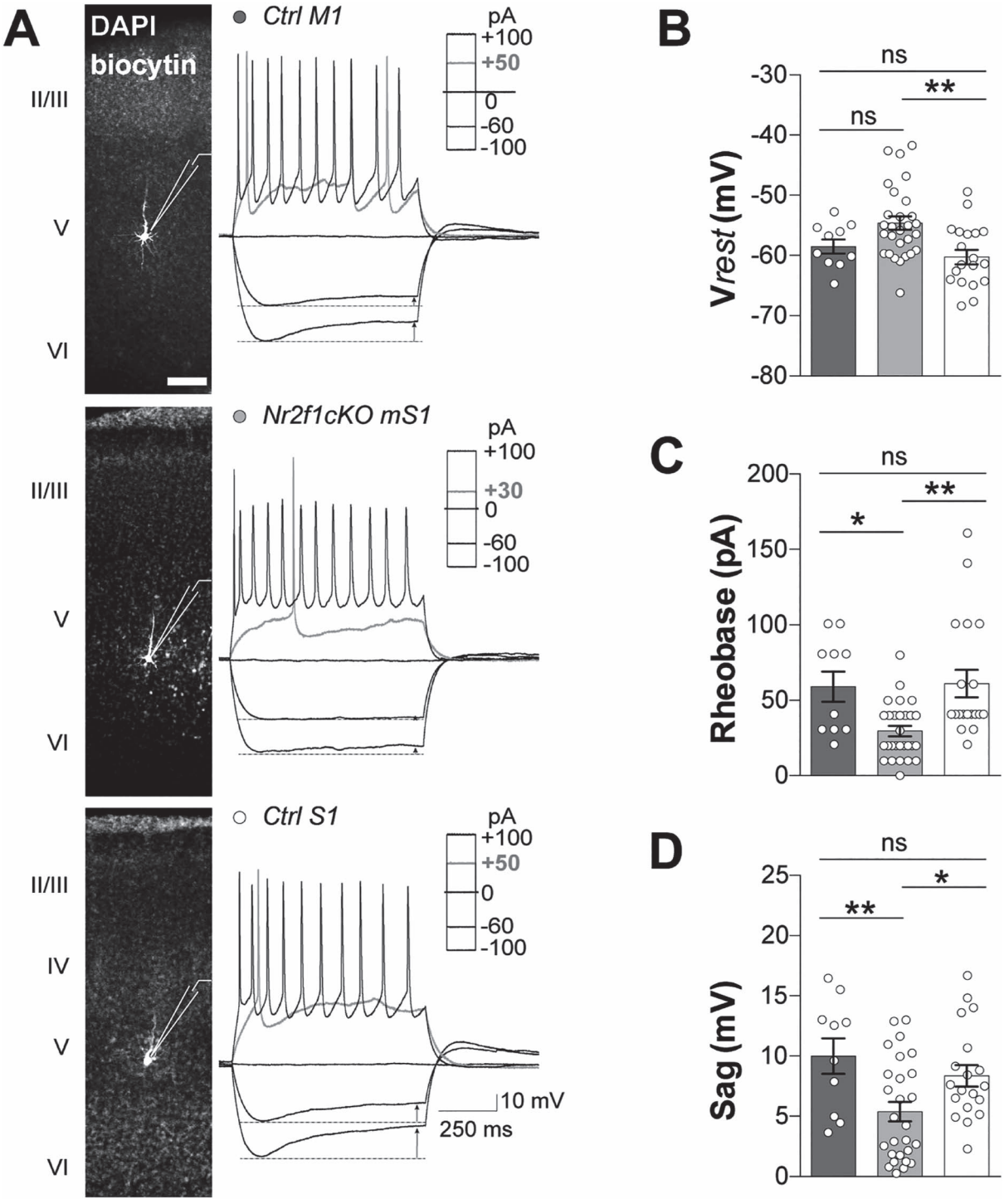

Figure 3. Abnormal intrinsic excitability of *Nr2f1*-deficient LVPNs. (*A*) LVPNs identified *post hoc* through fluorescent labeling for biocytin (in white) and DAPI (gray) in *Ctrl* M1, *Nr2f1cKO* mS1 and *Ctrl* S1 display slow-adapting regular spiking firing pattern. (*B*) Mean resting membrane potential (V_{rest}) is significantly different between the conditions (**$P = 0.0028$). Multiple comparisons show a significantly more depolarized V_{rest} in *Nr2f1cKO* mS1 than in *Ctrl* S1 neurons (**$P = 0.0025$) but not significantly different from M1 neurons ($P = 0.135$). (*C*) Rheobase is significantly different between the three conditions analyzed (**$P = 0.0017$). *Nr2f1cKO* mS1 pyramidal neurons display a significantly reduced rheobase compared to *Ctrl* M1 and S1 neurons (*$P = 0.004$ in M1 vs. mS1 and **$P = 0.003$ in S1 vs. mS1). (*D*) Sag is significantly different between the three conditions (**$P = 0.0063$). *Nr2f1cKO* mS1 neurons display a significantly lower sag response to hyperpolarization compared to *Ctrl* M1 (**$P = 0.0042$) and S1 neurons (*$P = 0.020$). Abbreviations: II, III, IV, V, VI, cortical layers II-VI. Sampling and statistical test listed in Supplementary Table 5. Data are represented as mean ± SEM. Scale bar: 100 µm. See also Supplementary Figure 3 and Supplementary Tables 2 and 5.

Downloaded from https://academic.oup.com/cercor/article-abstract/doi/10.1093/cercor/bhaa137/5860958 by University of Canberra user on 25 June 2020

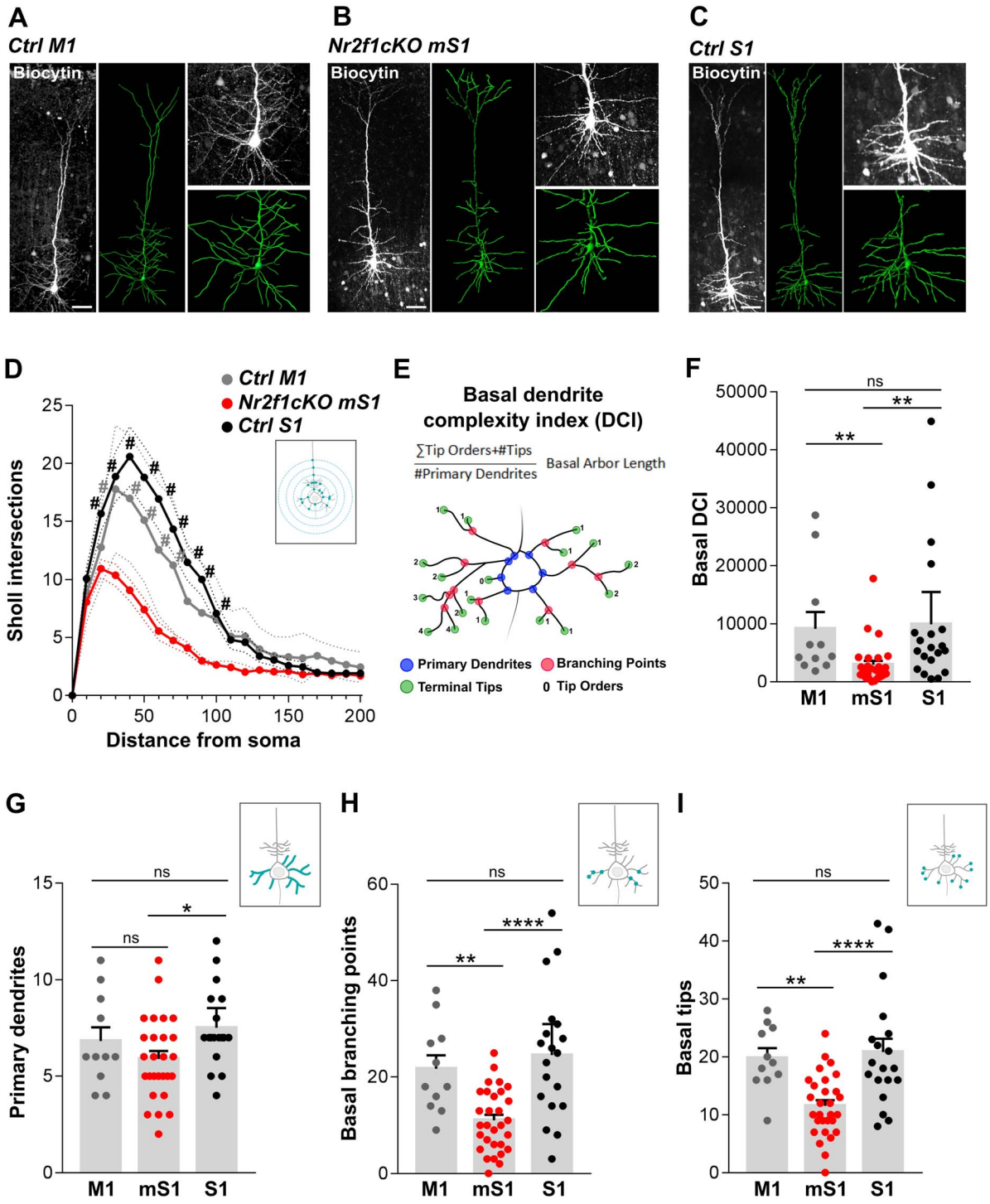

Figure 4. Reduced basal dendritic complexity of LVPNs in *Nr2f1* mutant cortices. Representative images of P7 *Ctrl* M1 (*A*), *Nr2f1cKO* mS1 (*B*), and *Ctrl* S1 (*C*) LVPNs. In grayscale, maximum intensity projection of a multistack confocal image; in green, correspondent 3D reconstructions. On the right, magnifications of the basal structures. Scale bar: 50 µm. (*D*) Sholl analysis points to a reduction of the arborization complexity in *Nr2f1cKO* mS1 LVPNs compared to both M1 and S1 control cells ($^{\#}P < 0.05$). For detailed statistics, see Supplementary Table 3. (*E*) Basal DCI formula and schematic representation of primary dendrites, branching points, terminal tips, and tip orders. (*F–I*) Average basal DCI (*Ctrl* M1, 9148 ± 2838; *Nr2f1cKO* mS1, 2956 ± 658; *Ctrl* S1, 9902 ± 2650; *Ctrl* S1 vs. *Nr2f1cKO* mS1, $P = 0.0025$; *Ctrl* M1 vs. *Nr2f1cKO* mS1, $P = 0.0063$), number of primary dendrites (*Ctrl* M1, 6.82 ± 0.71; *Nr2f1cKO* mS1, 5.89 ± 0.41; *Ctrl* S1, 7.5 ± 0.49; *Ctrl* S1 vs. *Nr2f1cKO* mS1, $P = 0.035$; *Ctrl* M1 vs. *Nr2f1cKO* mS1, $P = 0.41$), basal dendrites branching point (*Ctrl* M1, 21.73 ± 2.81; *Nr2f1cKO* mS1, 11.03 ± 1.17; *Ctrl* S1, 24.58 ± 3.05; *Ctrl* S1 vs. *Nr2f1cKO* mS1, $P = < 0.0001$; *Ctrl* M1 vs. *Nr2f1cKO* mS1, $P = 0.005$), and terminal tips (*Ctrl* M1, 19.82 ± 0.70; *Nr2f1cKO* mS1, 11.52 ± 0.99; *Ctrl* S1, 20.84 ± 2.265; *Ctrl* S1 vs. *Nr2f1cKO* mS1, $P \leq 0.0001$; *Ctrl* M1 vs. *Nr2f1cKO* mS1, $P = 0.0036$) are statistically reduced in mutant cells compared to controls. Data are represented as mean ± SEM. Sampling and statistical test listed in Supplementary Table 5. See also Supplementary Figure 3 and Supplementary Tables 3–5.

Downloaded from https://academic.oup.com/cercor/article-abstract/doi/10.1093/cercor/bhaa137/5860958 by University of Canberra user on 25 June 2020

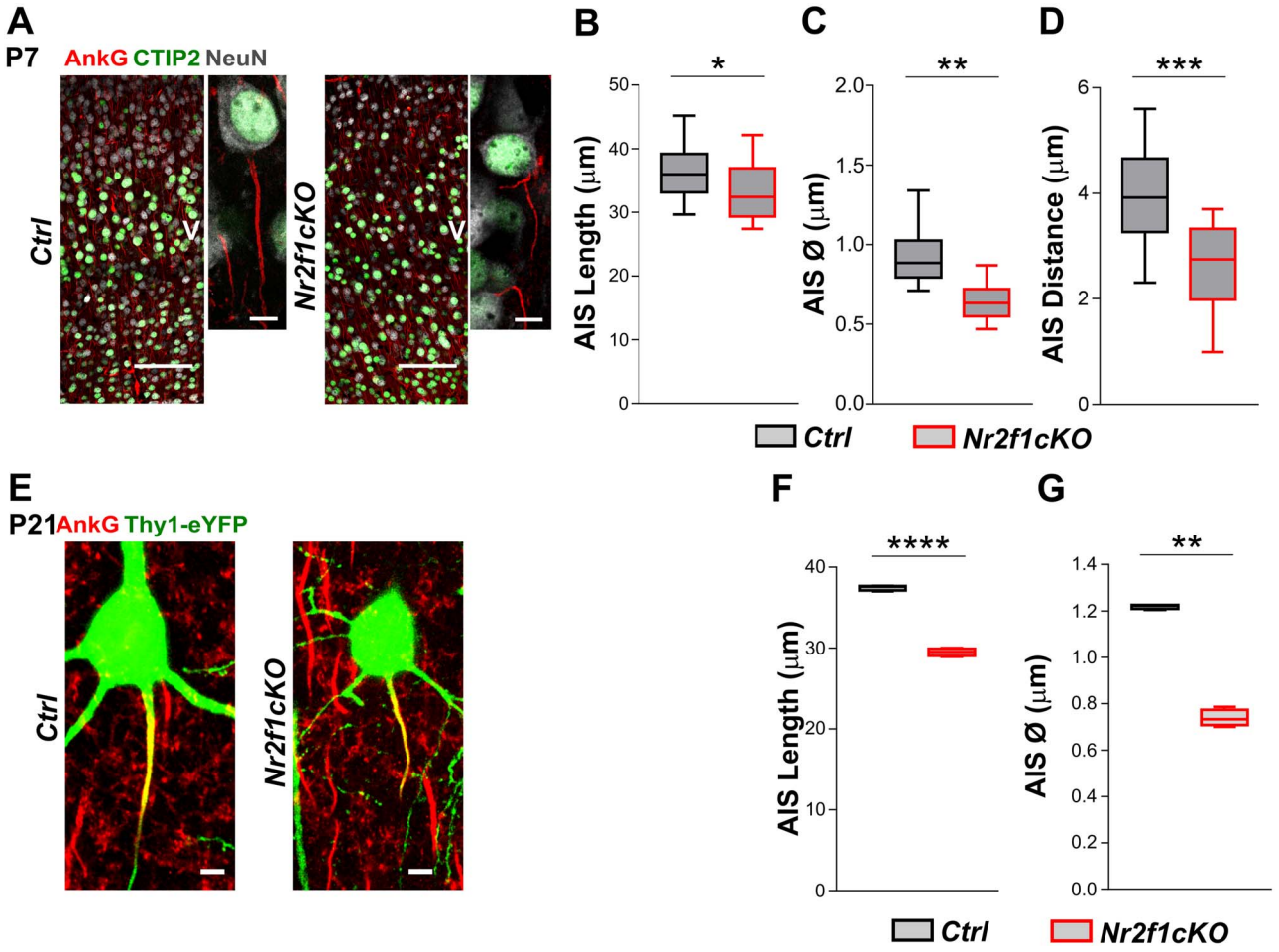

Figure 5. Abnormal structural features of the AIS in mutant *Nr2f1* LVPNs. (*A*) Left panel, coronal sections of P7 *Ctrl* S1 and *Nr2f1cKO* mS1 cortices labeled with CTIP2, for layer V identification, Ankyrin G for the AIS and NeuN as a somatic marker. Scale bar: 100 µm. Right panel confocal images of triple stained *Ctrl* and *Nr2f1cKO* LVPNs. Scale bar: 10 µm. (*B–D*) Average AIS length (*Ctrl*, 35.23 ± 0.67; *Nr2f1cKO*, 31.14 ± 0.32; $P = 0.0129$), diameter (*Ctrl*, 0.94 ± 0.006; *Nr2f1cKO*, 0.65 ± 0.004; $P = 0.0043$), and distance from the soma (*Ctrl*, 3.91 ± 0.21; *Nr2f1cKO*, 2.63 ± 0.2; $P = 0.0001$) are statistically reduced in *Nr2fcKO* neurons compared with *Ctrl* at P7. (*E*) Confocal images of *Ctrl* (left) and *Nr2f1cKO* (right) LVPNs from P21 somatosensory cortices. In green, *Thy1-eYFP* reporter gene; in red, Ankyrin G. (*F–G*) Average AIS length (*Ctrl*, 37.46 ± 0.15; *Nr2f1cKO*, 29.51 ± 0.23; $P < 0.0001$) and diameter (*Ctrl*, 1.2 ± 0.005; *Nr2f1cKO*, 0.74 ± 0.02; $P < 0.0001$) are statistically reduced in *Nr2f1cKO* cells compared with controls at P21. Data are represented as mean ± SEM. Sampling and statistical test listed in Supplementary Table 5. (See also Supplementary Fig. 5 and Supplementary Tables 4 and 5).

excitability through a modification of the expression of ion channels.

To this purpose, we performed RT-qPCR for an extensive list of K^+, Na^+, and Ca^{2+} channels specifically expressed in deep layers from *Ctrl* and *Nr2f1cKO* cortical lysates (Fig. 6A). Out of 33 ion channels that we could successfully test, we found a significant reduction in the *mRNA* levels of only *Hcn1*, *Kcnab1*, *Kcnk2*, *Cacna2d1*, *Gria3*, and *Grin1* in *Nr2f1cKO* when compared to *Ctrl* brains (Fig. 6A and Supplementary Fig. 6). Notably, we found significantly decreased protein levels of the hyperpolarization-activated cation channel HCN1 (Shah 2014) in *Nr2f1cKO* (Fig. 6B and Supplementary Fig. 7). Moreover, double staining of HCN1 and CTIP2 on cortical sections at P7, when HCN1 expression becomes detectable in cell bodies (Fig. 6C), confirmed decreased HCN1 protein signal intensity in CTIP2-expressing LVPNs, as well as a reduced number of double CTIP2/HCN1 positive neurons in mutant neurons compared to *Ctrls* (Fig. 6D,E), supporting overall reduction of HCN1 protein in layer V neurons of *Nr2f1cKO* mutant brains.

Finally, we investigated whether voltage-gated ion channels, whose transcript levels were found altered in mutant brains, were directly regulated by *Nr2f1*. To address this, we searched for evolutionary conserved binding sites for *Nr2f1* on the group of differentially expressed genes using the ECR browser tool (Ovcharenko et al. 2004; Loots and Ovcharenko 2007). By using MatInspector (Quandt et al. 1995) and ChromAnalyzer (Montemayor et al. 2010), we identified putative binding sites for *Nr2f1* at 25 kb of the 5'UTR of *Hcn1*, 3 kb of the 5'UTR of *Kcnab1*, and proximal to the 5'UTR of *Kcnd2* loci (Fig. 6F). These sites mainly match the *Nr2f1* canonical binding sequence consisting of direct repeats with variable spacer configurations, as previously described (Montemayor et al. 2010). Notably, we observed that the binding sequence on the *Hcn1* locus matched the expected consensus site (Fig. 6F, red nucleotides). To experimentally test the direct regulation of the expression of these ion channels by *Nr2f1*, we performed chromatin immunoprecipitation (ChIP) assay on whole newborn *Ctrl* cortices using a

Downloaded from https://academic.oup.com/cercor/article-abstract/doi/10.1093/cercor/bhaa137/5860958 by University of Canberra user on 25 June 2020

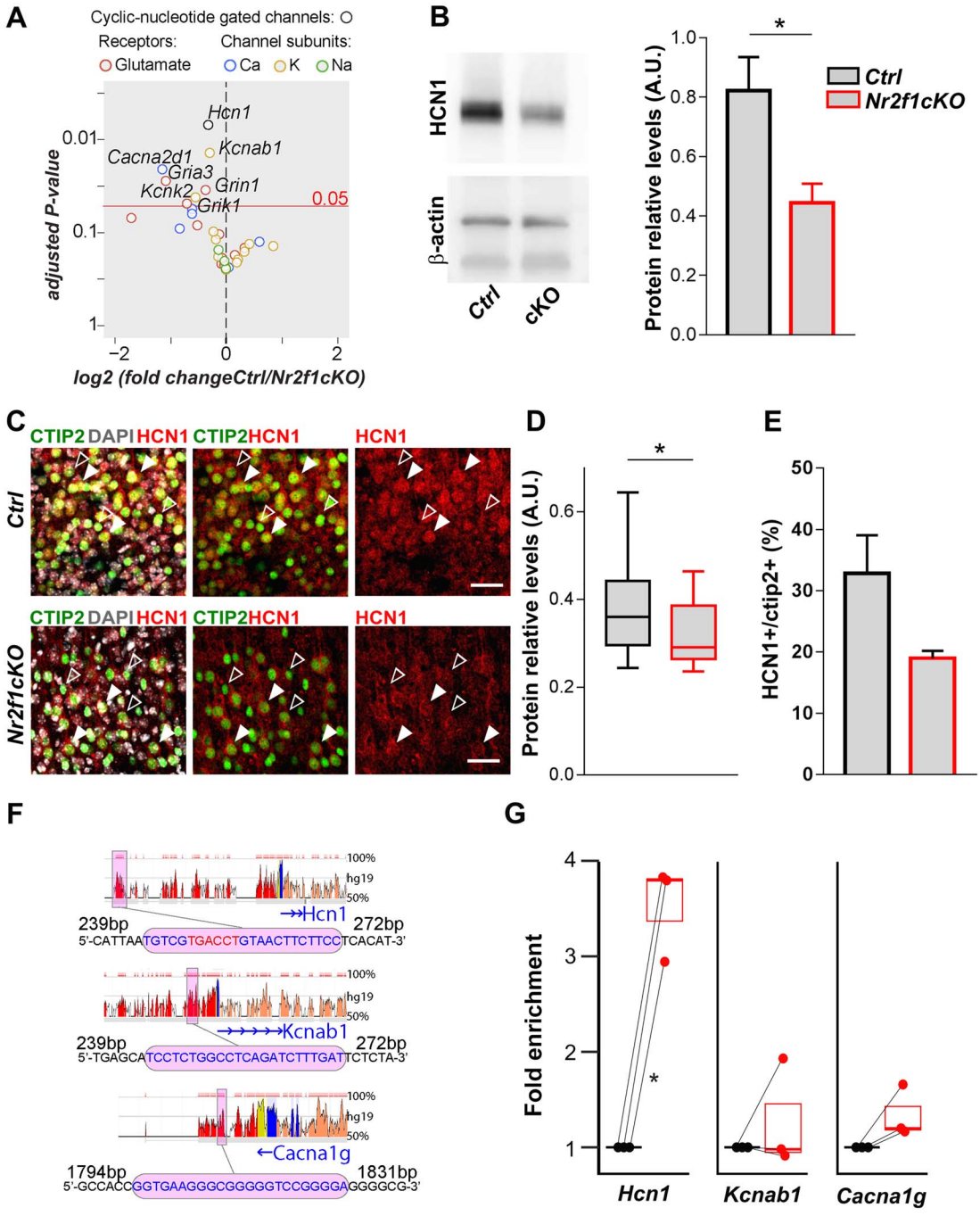

Figure 6. Regulation of ion channel-expression levels by *Nr2f1*. (*A*) Data plot of qPCR analysis on P7 *Ctrl* and *Nr2f1cKO* cortices. The red line represents the threshold for significance. Significantly downregulated genes are depicted in the upper left panel. (*B*) Western blot analysis of HCN1 protein shows a significant reduction in *Nr2f1cKO* P7 cortices (*Ctrl*, 0.822 ± 0.11; *Nr2f1cKO*, 0.44 ± 0.064; $P = 0.05$). (*C*) CTIP2-HCN1 double IF staining of P7 somatosensory cortices. (*D*) Box and whiskers plot distribution of HCN1 cell signal intensity points to a reduction of HCN1 in *Nr2f1cKO* LVPNs (*Ctrl*, 0.89 ± 0.03; *Nr2f1cKO*, 0.71 ± 0.01; $P = 0.015$). (*E*) The number of HCN1$^+$ cells within the LVPN CTIP2$^+$ population tends to be reduced in *Nr2f1cKO* cells (*Ctrl*, 32.81 ± 6.24; *Nr2f1cKO*, 18.99 ± 1.19; $P = 0.15$). (*F*) Snapshots from Evolutionary Conserved Regions browser showing Nr2f1 binding location and sites (in pink; red nucleotides highlighting the canonical direct repeat of *Nr2f1* binding site: TGACCT); intergenic regions (red); UTR (yellow); exons (blue); and introns (orange). (*G*) Immunoprecipitation of chromatin (ChIP) indicates that Nr2f1 binds these sites with different affinities. All data are expressed as "relative" fold enrichment and normalized against ChIP performed on the same samples with an anti-GFP as an aspecific antibody. Data are represented as mean ± SEM. Sampling and statistical test listed in Supplementary Table 5. See also Supplementary Figure 6 and Supplementary Tables 4 and 5.

Downloaded from https://academic.oup.com/cercor/article-abstract/doi/10.1093/cercor/bhaa137/5860958 by University of Canberra user on 25 June 2020

well-established Nr2f1 antibody (Alfano et al. 2011; Parisot et al. 2017). Quantitative PCR (qPCR) analysis of immunoprecipitated material showed a reproducible 3- to 4-fold significant enrichment of Nr2f1 *versus* GFP unspecific binding only on the *Hcn1* locus and not on the *Kcnab1* or *Cacna1g* loci (Fig. 6G), despite their altered transcript levels quantified in mutant brains (Supplementary Fig. 6). These data on the molecular landscape of the somatosensory cortex indicate that while expression levels of several ion channels might be modulated by Nr2f1 during cortical development, only few of them seem to be directly controlled by this factor. We thus hypothesize that the changes in neuronal activity induced by Nr2f1 can have secondary consequences for a number of activity-dependent neuronal and network maturation processes. Overall, we identified *Hcn1* gene, whose protein product is known to determine voltage sag and intrinsic excitability, as one of several putative direct targets (Brager et al. 2012; Zhang et al. 2014; Fan et al. 2016).

Discussion

Our work reveals early developmental alterations in spontaneous activity and intrinsic excitability of the neocortex in a mouse model of cortical patterning abnormalities. We propose that *Nr2f1* expression within the immature S1 cortex is required for the emergence of S1 area-specific features that go beyond molecular and topographic connectivity, as previously reported (Armentano et al. 2007; Alfano et al. 2014). Here, we show that Nr2f1 does not only play a key role in imparting somatosensory identity to young neurons (Alfano et al. 2014), but that it also regulates the development of proper neocortical activity patterns and bioelectrical properties. Therefore, our data provide an additional link between intrinsic genetic determination of proto-areas and spontaneous cortical activity in the immature cortex through the regulation of membrane ion channels in glutamatergic pyramidal neurons (summarized in Fig. 7).

Cortical and Thalamic Early Developmental Activity Governing Proper Formation of Somatosensory Maps

In this study, we show that loss of cortical Nr2f1, known to determine sensory identity of early differentiating neurons (Alfano et al. 2014), also impacts on intrinsic network activity within the immature neocortex. These findings indicate that, in addition to acquiring motor-like properties in terms of early molecular fate specification, mS1 neurons undergo unique changes in intrinsic electrophysiological properties in a manner that is different from S1 but also distinct from M1 electrophysiological identities.

A recent study reports that prenatal activity of thalamic neurons can influence somatosensory map formation in the cortex before the emergence of sensory inputs (Anton-Bolanos et al. 2019). Upon blockade of thalamic calcium waves, the neocortex becomes hyperexcitable, the columnar and barrel organizations are perturbed, and the somatosensory map lacks anatomical and functional structure. Perturbation of laminar and columnar development of the barrel cortex has also been observed in transgenic mice in which glutamatergic release was disrupted in thalamocortical axons (Li et al. 2013). This could imply that impaired organization of the somatosensory map observed in *Nr2f1cKO* mutants is caused by the absence of prenatal thalamic inputs reaching the mutant cortex. This hypothesis, however, is not entirely supported by our data, since thalamic axons do reach the subplate in *Nr2f1* mutant prenatal cortices (Armentano et al. 2007). Nevertheless, thalamocortical interactions in *Nr2f1* mutants may be dysfunctional due to pre- or postsynaptic mechanisms. For example, presynaptic alterations of incoming thalamocortical axons may be due to the altered expression of cortical molecular cues. A nonexclusive, interesting hypothesis that arises from our results, is that of altered properties of postsynaptic mis-differentiated S1 neurons in *Nr2f1* mutant cortices. We have demonstrated that neuronal intrinsic properties, morphology, and spontaneous activity are altered in the S1 region of mutant brains at a critical period for thalamocortical interactions that are crucial for proper laminar and columnar development of the barrel cortex. Hence, the early expression of arealization genes, such as *Nr2f1*, might be necessary to set up proper postsynaptic properties and synchronized activity patterns within the immature somatosensory cortex.

Nr2f1 Controls Determinants of Spontaneous Network Activity

Developmental spontaneous activity has already been described to follow a regionalized pattern in the cortex (Corlew et al. 2004; Uhlen et al. 2015) and to ultimately influence the assembly of long-range circuit connections (Tritsch et al. 2007; Blankenship et al. 2011; Yamamoto and Lopez-Bendito 2012; Schneggenburger and Rosenmund 2015; Anton-Bolanos et al. 2019). However, how spontaneous activity is first triggered and then finely modulated during the formation of the neocortical protomap is still unclear. In the mouse neocortex, large plateaus of synchronized network activity at birth are followed by early network oscillations and giant depolarizing potentials during the first postnatal week (Allene et al. 2008; Allene and Cossart 2010). Multiple aspects that relate to intrinsically regulated maturation of pyramidal neurons might influence the developmental sequence of cortical network activity. Our data provide a novel characterization at electrophysiological and molecular levels of intrinsic excitability features in S1 that are influenced by abnormal patterning of the somatosensory cortex in the absence of *Nr2f1* during the first postnatal week. Our hypothesis that *Nr2f1* expression could influence molecular determinants relevant for early neuronal network activity is corroborated by previous transcriptome analyses. Indeed, *Nr2f1* loss in postmitotic cortical cells regulates the expression of several activity-related genes, such as *Chrna7, Kcnq3, Kcnlp4, Robo1*, and *Sv2b* (Alfano et al. 2014). However, the direct impact of these candidates on immature cortical neuron activity still remains to be investigated.

Several studies have also highlighted the role of cell intrinsic and presynaptic factors in determining cortical network development with potential long-term effects (Boillot et al. 2016; Murase et al. 2016). For example, the transcription factor Tbr1, known to regulate cortical layer identity, also alters the intrinsic excitability of neocortical neurons, by regulating HCN1 transcription in neonates and increasing sag response in layer VI (Fazel Darbandi et al. 2018). Thus, among several possible pathways involving ion channels, regulation of HCN1 levels is potentially an example of common mechanisms used by early transcriptional regulators to modulate spontaneous network activity within the developing cortex.

Within immature cortical networks, the earliest patterns of correlated spontaneous activity (synchronous plateau assemblies) are thought to arise from voltage-gated conductance and

Downloaded from https://academic.oup.com/cercor/article-abstract/doi/10.1093/cercor/bhaa137/5860958 by University of Canberra user on 25 June 2020

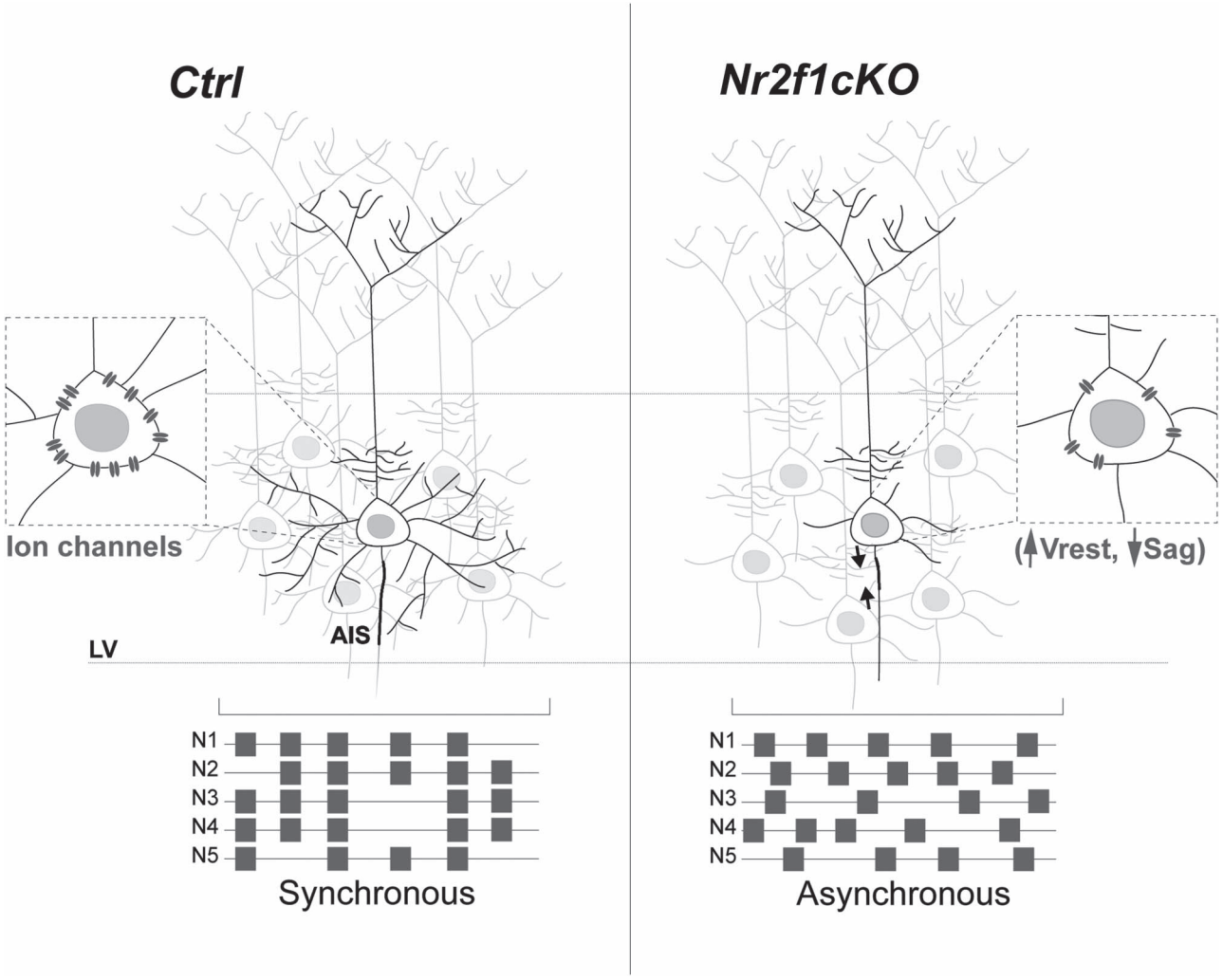

Figure 7. Schematics summarizing the changes in pyramidal neuron anatomy, bioelectric properties, and network synchronization upon Nr2f1 loss. The summary schema highlights a pyramidal neuron with less complex basal dendritic arbor, shorter AIS (in black), and reduced expression of ion channels (in the inset, in dark gray), leading to altered resting membrane potential (V_{rest}) and sag ratio (Sag) as well as asynchronous firing of neurons (below) within the cortical network of the immature somatosensory area, in the absence of *Nr2f1* (*Nr2f1cKO*) compared with a *Ctrl* neuron. Arrows point to the length of the AIS, which is reduced in mutant neurons.

gap junction coupling (Roerig and Feller 2000; Pearson et al. 2004; Allene et al. 2008; Blankenship et al. 2011; Cho and Choi 2012). These early events are followed by cortical early network oscillations (cENOs) generated by a glutamatergic synaptic and extrasynaptic drive (Garaschuk et al. 1998; Allene et al. 2008). In this context, it is important to note that *Nr2f1* loss also affects the expression of GRIN1 and many cell-adhesion-related genes (i.e., *Cdh4*, *Cdh11*, *Cdh12*, *Fat3*, and *Ncam2*) (Alfano et al. 2014). These could in turn impair gap-junction functionality, glutamatergic signaling, and therefore the expression of synchronous plateau assemblies and cENOs. Interestingly, intrinsic bioelectrical membrane properties prominently determine the occurrence of membrane potential spikes before gap-junction coupling takes place (Allene and Cossart 2010). Hence, it is tempting to speculate that *Nr2f1* function might involve early forms of activity within the embryonic brain together with regulating fate-specific determinants.

Concomitant Changes in Intrinsic Neural Excitability during Nr2f1-Dependent Neocortical Development

Our study reports several alterations of pyramidal glutamatergic neuron intrinsic properties, presumably due to the altered expression of HCN1 and other ion channels, such as the ones identified in our study (Kcnab1, Grin1, Gria3 Cacna2d1, and Kcnk2). Functionally, we have observed a reduced I_h and associated voltage sag, and other changes pointing to increased neuronal excitability, such as a more depolarized resting membrane potential (V_{rest}) and an increased maximum firing frequency. In mature glutamatergic neurons of the adult rodent neocortex, HCN1 is prominently localized to apical dendrites and regulates dendritic calcium electrogenesis, intrinsic high frequency, burst, and sustained firing (Kole et al. 2007; Thuault et al. 2013; Zhang et al., 2014). Its blockade results in a more hyperpolarized resting membrane potential but increased membrane resistance,

Downloaded from https://academic.oup.com/cercor/article-abstract/doi/10.1093/cercor/bhaa137/5860958 by University of Canberra user on 25 June 2020

synaptic integration, and AP back-propagation efficacy, as previously described (Magee 1998; Williams and Stuart 2000; Berger et al. 2001; Chen et al. 2001; Lupica et al. 2001; Poolos et al. 2002; Wang et al. 2003; Williams and Stuart 2003; Nolan et al. 2004; Fan et al. 2005; Poolos et al. 2006; van Welie et al. 2006; Brager and Johnston 2007; Bender and Baram 2008; Zhang et al., 2014). In addition, intrinsic pacemaker properties through HCN1 expression have been hypothesized to generate and drive distinct synchronized activity patterns in immature networks (Luhmann et al. 2016).

Another factor that could lead to abnormal excitability is delayed maturation of pyramidal cells as a result of *Nr2f1* loss. Indeed, in our *ex vivo* electrophysiological analysis, some properties of *Nr2f1cKO* LVPNs, such as membrane resting potential, resemble those of less mature neurons. In contrast, other electrophysiological parameters, such as input resistance and capacitance, do not reflect any delay in maturation. Moreover, our analysis of AIS plasticity at P21 also does not indicate a maturation defect in individual neurons but rather favors the hypothesis of a homeostatic/compensatory effect leading to decreased dendritic complexity and AIS plasticity.

Finally, genetic or pharmacological dysfunction in HCN channels in mice results in behavioral phenotypes associated with somatosensory-motor coordination, for example, reduced forelimb reaching accuracy and atypical movements during a single-pellet skill reaching task (Boychuk et al. 2017). Similar behavioral phenotypes are displayed by *Nr2f1cKO* mice (Tomassy et al. 2010) and resemble symptoms of *NR2F1* haploinsufficient patients (Bosch et al. 2014; Chen et al. 2016; Rech et al. 2020). Together with the cellular and molecular role of Nr2f1 during intrinsic area patterning, this study has unraveled neuronal intrinsic excitability and spontaneous activity as novel aspects of the phenotype related to reduced *Nr2f1* expression. These might prove useful to better understand axonal connectivity and circuit formation leading to abnormal behavior and cortical dysfunction in mice (Tomassy et al. 2010; Flore et al. 2017; Contesse et al. 2019) and in humans (Bosch et al. 2016; Chen et al. 2016; Rech et al., 2020).

Supplementary Material

Supplementary material is available at *Cerebral Cortex* online.

Author Contributions

Conceptualization, methodology, validation, and formal analysis, I.D.P., C.T., E.M., A.M., C.A., M.S., X.L., and A.F.; investigation, I.D.P., C.T., E.M., A.M., C.F., M.B., and G.T.; resources, M.S. and A.F.; writing—original draft and editing, I.D.P., C.T., E.M., A.M., and M.S.; writing—review, X.L. and A.F.; visualization, I.D.P., C.T., E.M., and A.M.; funding acquisition, M.S., X.L., A.F., and I.D.P.

Funding

Agence National de la Recherche (grant # ANR-13-BSV4-0011-01 to M.S. and X.L.); Fondation Recherche Médicale; Equipe FRM 2015 (grant #DEQ20150331750 to M.S.) and 4th year FRM PhD fellowship #FDT201904008137 to C.T.; "Investments for the Future" LabEx SIGNALIFE (grant ANR-11-LABX-0028-01 to M.S.); Région PACA PhD fellowship (project R16097AA-CR PACA/Inserm 2016) to C.T. "Initiative d'Excellence (IdEx) de l'Université de Bordeaux" fellowship and Spanish Ministry of Science, Innovation and Universities RTI2018-100872-J-I00 to I.D.P.; Inserm endowment to A.F.

Notes

We thank Dr M. Kole and Dr. N Dehorter for critical reading of the manuscript and members of the Studer and Frick laboratories for stimulating discussions. We also thank G. Lopez-Bendito for insightful suggestions. We are grateful to the iBV PRISM Microscopy facility and the Bordeaux Imaging Center, supported by Labex-BRAIN (ANR-10-LABEX-43), for the acquisition of some imaging data. The authors also thank the animal and genotyping facilities of the Neurocentre Magendie (supported by INSERM and LabEX-BRAIN ANR-10-LABX-43) and of the iBV.

Conflict of Interest: The corresponding author declares nonfinancial competing interest on behalf of all authors.

References

Alfano C, Magrinelli E, Harb K, Hevner RF, Studer M. 2014. Postmitotic control of sensory area specification during neocortical development. *Nat Commun*. 5:5632.

Alfano C, Studer M. 2012. Neocortical arealization: evolution, mechanisms and open questions. *Dev Neurobiol*. 73:411–447.

Alfano C, Viola L, Heng JI, Pirozzi M, Clarkson M, Flore G, De Maio A, Schedl A, Guillemot F, Studer M. 2011. COUP-TFI promotes radial migration and proper morphology of callosal projection neurons by repressing Rnd2 expression. *Development*. 138:4685–4697.

Allene C, Cattani A, Ackman JB, Bonifazi P, Aniksztejn L, Ben-Ari Y, Cossart R. 2008. Sequential generation of two distinct synapse-driven network patterns in developing neocortex. *J Neurosci*. 28:12851–12863.

Allene C, Cossart R. 2010. Early NMDA receptor-driven waves of activity in the developing neocortex: physiological or pathological network oscillations? *J Physiol*. 588:83–91.

Allio A, Calorio C, Franchino C, Gavello D, Carbone E, Marcantoni A. 2015. Bud extracts from Tilia tomentosa Moench inhibit hippocampal neuronal firing through GABAA and benzodiazepine receptors activation. *J Ethnopharmacol*. 172:288–296.

Anderson OD. 1975. Moving average processes. *Statistician*. 24:283–297.

Andreae LC, Burrone J. 2018. The role of spontaneous neurotransmission in synapse and circuit development. *J Neurosci Res*. 96:354–359.

Anton-Bolanos N, Sempere-Ferrandez A, Guillamon-Vivancos T, Martini FJ, Perez-Saiz L, Gezelius H, Filipchuk A, Valdeolmillos M, Lopez-Bendito G. 2019. Prenatal activity from thalamic neurons governs the emergence of functional cortical maps in mice. *Science*. 364:987–990.

Arlotta P, Molyneaux BJ, Chen J, Inoue J, Kominami R, Macklis JD. 2005. Neuronal subtype-specific genes that control corticospinal motor neuron development in vivo. *Neuron*. 45:207–221.

Armentano M, Chou SJ, Tomassy GS, Leingartner A, O'Leary DD, Studer M. 2007. COUP-TFI regulates the balance of cortical patterning between frontal/motor and sensory areas. *Nat Neurosci*. 10:1277–1286.

Bender RA, Baram TZ. 2008. Hyperpolarization activated cyclic-nucleotide gated (HCN) channels in developing neuronal networks. *Prog Neurobiol*. 86:129–140.

Berger T, Larkum ME, Luscher HR. 2001. High I(h) channel density in the distal apical dendrite of layer V pyramidal cells

Downloaded from https://academic.oup.com/cercor/article-abstract/doi/10.1093/cercor/bhaa137/5860958 by University of Canberra user on 25 June 2020

increases bidirectional attenuation of EPSPs. *J Neurophysiol*. 85:855–868.

Bertacchi M, Parisot J, Studer M. 2019. The pleiotropic transcriptional regulator COUP-TFI plays multiple roles in neural development and disease. *Brain Res*. 1705:75–94.

Blankenship AG, Hamby AM, Firl A, Vyas S, Maxeiner S, Willecke K, Feller MB. 2011. The role of neuronal connexins 36 and 45 in shaping spontaneous firing patterns in the developing retina. *J Neurosci*. 31:9998–10008.

Boillot M, Lee CY, Allene C, Leguern E, Baulac S, Rouach N. 2016. LGI1 acts presynaptically to regulate excitatory synaptic transmission during early postnatal development. *Sci Rep*. 6:21769.

Bosch DG, Boonstra FN, de Leeuw N, Pfundt R, Nillesen WM, de Ligt J, Gilissen C, Jhangiani S, Lupski JR, Cremers FP *et al*. 2016. Novel genetic causes for cerebral visual impairment. *Eur J Hum Genet*. 24:660–665.

Bosch DG, Boonstra FN, Gonzaga-Jauregui C, Xu M, de Ligt J, Jhangiani S, Wiszniewski W, Muzny DM, Yntema HG, Pfundt R *et al*. 2014. NR2F1 mutations cause optic atrophy with intellectual disability. *Am J Hum Genet*. 94:303–309.

Boychuk JA, Farrell JS, Palmer LA, Singleton AC, Pittman QJ, Teskey GC. 2017. HCN channels segregate stimulation-evoked movement responses in neocortex and allow for coordinated forelimb movements in rodents. *J Physiol*. 595:247–263.

Brager DH, Akhavan AR, Johnston D. 2012. Impaired dendritic expression and plasticity of h-channels in the fmr1(−/y) mouse model of fragile X syndrome. *Cell Rep*. 1:225–233.

Brager DH, Johnston D. 2007. Plasticity of intrinsic excitability during long-term depression is mediated through mGluR-dependent changes in I(h) in hippocampal CA1 pyramidal neurons. *J Neurosci*. 27:13926–13937.

Cadwell CR, Bhaduri A, Mostajo-Radji MA, Keefe MG, Nowakowski TJ. 2019. Development and arealization of the cerebral cortex. *Neuron*. 103:980–1004.

Chen CA, Bosch DG, Cho MT, Rosenfeld JA, Shinawi M, Lewis RA, Mann J, Jayakar P, Payne K, Walsh L *et al*. 2016. The expanding clinical phenotype of Bosch-Boonstra-Schaaf optic atrophy syndrome: 20 new cases and possible genotype-phenotype correlations. *Genet Med*. 18:1143–1150.

Chen K, Aradi I, Thon N, Eghbal-Ahmadi M, Baram TZ, Soltesz I. 2001. Persistently modified h-channels after complex febrile seizures convert the seizure-induced enhancement of inhibition to hyperexcitability. *Nat Med*. 7:331–337.

Cho MW, Choi MY. 2012. Spontaneous organization of the cortical structure through endogenous neural firing and gap junction transmission. *Neural Netw*. 31:46–52.

Christophe E, Doerflinger N, Lavery DJ, Molnar Z, Charpak S, Audinat E. 2005. Two populations of layer v pyramidal cells of the mouse neocortex: development and sensitivity to anesthetics. *J Neurophysiol*. 94:3357–3367.

Computing RFfS. 2018. *R: A Language and Environment for Statistical Computing*. R Foundation for Statistical Computing, In.

Contesse T, Ayrault M, Mantegazza M, Studer M, Deschaux O. 2019. Hyperactive and anxiolytic-like behaviors result from loss of COUP-TFI/Nr2f1 in the mouse cortex. *Genes Brain Behav*. 18:e12556.

Corlew R, Bosma MM, Moody WJ. 2004. Spontaneous, synchronous electrical activity in neonatal mouse cortical neurones. *J Physiol*. 560:377–390.

Cotterill E, Charlesworth P, Thomas CW, Paulsen O, Eglen SJ. 2016. A comparison of computational methods for detecting bursts in neuronal spike trains and their application to human stem cell-derived neuronal networks. *J Neurophysiol*. 116:306–321.

Del Pino I, Brotons-Mas JR, Marques-Smith A, Marighetto A, Frick A, Marin O, Rico B. 2017. Abnormal wiring of CCK(+) basket cells disrupts spatial information coding. *Nat Neurosci*. 20:784–792.

Del Pino I, Garcia-Frigola C, Dehorter N, Brotons-Mas JR, Alvarez-Salvado E, Martinez de Lagran M, Ciceri G, Gabaldon MV, Moratal D, Dierssen M *et al*. 2013. Erbb4 deletion from fast-spiking interneurons causes schizophrenia-like phenotypes. *Neuron*. 79:1152–1168.

Dumitrescu AS, Evans MD, Grubb MS. 2016. Evaluating tools for live imaging of structural plasticity at the axon initial segment. *Front Cell Neurosci*. 10:268.

Fan J, Stemkowski PL, Gandini MA, Black SA, Zhang Z, Souza IA, Chen L, Zamponi GW. 2016. Reduced hyperpolarization-activated current contributes to enhanced intrinsic excitability in cultured hippocampal neurons from PrP(−/−) mice. *Front Cell Neurosci*. 10:74.

Fan Y, Fricker D, Brager DH, Chen X, Lu HC, Chitwood RA, Johnston D. 2005. Activity-dependent decrease of excitability in rat hippocampal neurons through increases in I(h). *Nat Neurosci*. 8:1542–1551.

Favuzzi E, Deogracias R, Marques-Smith A, Maeso P, Jezequel J, Exposito-Alonso D, Balia M, Kroon T, Hinojosa AJ, E FM *et al*. 2019. Distinct molecular programs regulate synapse specificity in cortical inhibitory circuits. *Science*. 363:413–417.

Fazel Darbandi S, Robinson Schwartz SE, Qi Q, Catta-Preta R, Pai EL, Mandell JD, Everitt A, Rubin A, Krasnoff RA, Katzman S *et al*. 2018. Neonatal Tbr1 dosage controls cortical layer 6 connectivity. *Neuron*. 100:831–845.e837.

Flore G, Di Ruberto G, Parisot J, Sannino S, Russo F, Illingworth EA, Studer M, De Leonibus E. 2017. Gradient COUP-TFI expression is required for functional Organization of the Hippocampal Septo-Temporal Longitudinal Axis. *Cereb Cortex*. 27:1629–1643.

Garaschuk O, Hanse E, Konnerth A. 1998. Developmental profile and synaptic origin of early network oscillations in the CA1 region of rat neonatal hippocampus. *J Physiol*. 507(Pt 1):219–236.

Gavello D, Calorio C, Franchino C, Cesano F, Carabelli V, Carbone E, Marcantoni A. 2018. Early alterations of hippocampal neuronal firing induced by Abeta42. *Cereb Cortex*. 28:433–446.

Gavello D, Rojo-Ruiz J, Marcantoni A, Franchino C, Carbone E, Carabelli V. 2012. Leptin counteracts the hypoxia-induced inhibition of spontaneously firing hippocampal neurons: a microelectrode array study. *PLoS One*. 7:e41530.

Greig LC, Woodworth MB, Galazo MJ, Padmanabhan H, Macklis JD. 2013. Molecular logic of neocortical projection neuron specification, development and diversity. *Nat Rev Neurosci*. 14:755–769.

Grubb MS, Burrone J. 2010. Activity-dependent relocation of the axon initial segment fine-tunes neuronal excitability. *Nature*. 465:1070–1074.

Gulledge AT, Bravo JJ. 2016. Neuron morphology influences axon initial segment plasticity. *eNeuro*. 3:ENEURO.0085-15.2016. doi: 10.1523/ENEURO.0085-15.2016.

Hamada MS, Goethals S, de Vries SI, Brette R, Kole MH. 2016. Covariation of axon initial segment location and dendritic tree normalizes the somatic action potential. *Proc Natl Acad Sci U S A*. 113:14841–14846.

Downloaded from https://academic.oup.com/cercor/article-abstract/doi/10.1093/cercor/bhaa137/5860958 by University of Canberra user on 25 June 2020

Harb K, Magrinelli E, Nicolas CS, Lukianets N, Frangeul L, Pietri M, Sun T, Sandoz G, Grammont F, Jabaudon D *et al*. 2016. Area-specific development of distinct projection neuron subclasses is regulated by postnatal epigenetic modifications. *Elife*. 5:e09531.

Jabaudon D. 2017. Fate and freedom in developing neocortical circuits. *Nat Commun*. 8:16042.

Kasper EM, Larkman AU, Lubke J, Blakemore C. 1994. Pyramidal neurons in layer 5 of the rat visual cortex. II. Development of electrophysiological properties. *J Comp Neurol*. 339: 475–494.

Kirischuk S, Sinning A, Blanquie O, Yang JW, Luhmann HJ, Kilb W. 2017. Modulation of neocortical development by early neuronal activity: physiology and pathophysiology. *Front Cell Neurosci*. 11:379.

Kirkby LA, Sack GS, Firl A, Feller MB. 2013. A role for correlated spontaneous activity in the assembly of neural circuits. *Neuron*. 80:1129–1144.

Kole MH, Brauer AU, Stuart GJ. 2007. Inherited cortical HCN1 channel loss amplifies dendritic calcium electrogenesis and burst firing in a rat absence epilepsy model. *J Physiol*. 578:507–525.

Kole MH, Stuart GJ. 2012. Signal processing in the axon initial segment. *Neuron*. 73:235–247.

Kordeli E, Lambert S, Bennett V. 1995. AnkyrinG, A new ankyrin gene with neural-specific isoforms localized at the axonal initial segment and node of Ranvier. *J Biol Chem*. 270:2352–2359.

Kuba H. 2010. Plasticity at the axon initial segment. *Commun Integr Biol*. 3:597–598.

Kuba H, Oichi Y, Ohmori H. 2010. Presynaptic activity regulates Na(+) channel distribution at the axon initial segment. *Nature*. 465:1075–1078.

Li H, Fertuzinhos S, Mohns E, Hnasko TS, Verhage M, Edwards R, Sestan N, Crair MC. 2013. Laminar and columnar development of barrel cortex relies on thalamocortical neurotransmission. *Neuron*. 79:970–986.

Loots G, Ovcharenko I. 2007. ECRbase: database of evolutionary conserved regions, promoters, and transcription factor binding sites in vertebrate genomes. *Bioinformatics*. 23: 122–124.

Luhmann HJ, Khazipov R. 2018. Neuronal activity patterns in the developing barrel cortex. *Neuroscience*. 368: 256–267.

Luhmann HJ, Sinning A, Yang JW, Reyes-Puerta V, Stuttgen MC, Kirischuk S, Kilb W. 2016. Spontaneous neuronal activity in developing neocortical networks: from single cells to large-scale interactions. *Front Neural Circuits*. 10:40.

Lupica CR, Bell JA, Hoffman AF, Watson PL. 2001. Contribution of the hyperpolarization-activated current (I(h)) to membrane potential and GABA release in hippocampal interneurons. *J Neurophysiol*. 86:261–268.

Magee JC. 1998. Dendritic hyperpolarization-activated currents modify the integrative properties of hippocampal CA1 pyramidal neurons. *J Neurosci*. 18:7613–7624.

Massengill JL, Smith MA, Son DI, O'Dowd DK. 1997. Differential expression of K4-AP currents and Kv3.1 potassium channel transcripts in cortical neurons that develop distinct firing phenotypes. *J Neurosci*. 17:3136–3147.

Montemayor C, Montemayor OA, Ridgeway A, Lin F, Wheeler DA, Pletcher SD, Pereira FA. 2010. Genome-wide analysis of binding sites and direct target genes of the orphan nuclear receptor NR2F1/COUP-TFI. *PLoS One*. 5:e8910.

Moody WJ, Bosma MM. 2005. Ion channel development, spontaneous activity, and activity-dependent development in nerve and muscle cells. *Physiol Rev*. 85:883–941.

Murase S, Lantz CL, Kim E, Gupta N, Higgins R, Stopfer M, Hoffman DA, Quinlan EM. 2016. Matrix Metalloproteinase-9 regulates neuronal circuit development and excitability. *Mol Neurobiol*. 53:3477–3493.

Nolan MF, Malleret G, Dudman JT, Buhl DL, Santoro B, Gibbs E, Vronskaya S, Buzsaki G, Siegelbaum SA, Kandel ER *et al*. 2004. A behavioral role for dendritic integration: HCN1 channels constrain spatial memory and plasticity at inputs to distal dendrites of CA1 pyramidal neurons. *Cell*. 119: 719–732.

O'Leary DD, Sahara S. 2008. Genetic regulation of arealization of the neocortex. *Curr Opin Neurobiol*. 18:90–100.

Ovcharenko I, Nobrega MA, Loots GG, Stubbs L. 2004. ECR browser: a tool for visualizing and accessing data from comparisons of multiple vertebrate genomes. *Nucleic Acids Res*. 32:W280–W286.

Parisot J, Flore G, Bertacchi M, Studer M. 2017. COUP-TFI mitotically regulates production and migration of dentate granule cells and modulates hippocampal Cxcr4 expression. *Development*. 144:2045–2058.

Pearson RA, Catsicas M, Becker DL, Bayley P, Luneborg NL, Mobbs P. 2004. Ca(2+) signalling and gap junction coupling within and between pigment epithelium and neural retina in the developing chick. *Eur J Neurosci*. 19:2435–2445.

Poolos NP, Bullis JB, Roth MK. 2006. Modulation of h-channels in hippocampal pyramidal neurons by p38 mitogen-activated protein kinase. *J Neurosci*. 26:7995–8003.

Poolos NP, Migliore M, Johnston D. 2002. Pharmacological upregulation of h-channels reduces the excitability of pyramidal neuron dendrites. *Nat Neurosci*. 5:767–774.

Quandt K, Frech K, Karas H, Wingender E, Werner T. 1995. MatInd and MatInspector: new fast and versatile tools for detection of consensus matches in nucleotide sequence data. *Nucleic Acids Res*. 23:4878–4884.

Rech ME, McCarthy JM, Chen C-A, Edmond JC, Shah VS, Bosch DGM, Berry GT, Williams L, Madan-Khetarpal S, Niyazov D *et al*. Phenotypic expansion of Bosch-Boonstra-Schaaf optic atrophy syndrome and further evidence for genotype-phenotype correlations. *Am. J. Med. Genet. A*. https://doi.org/10.1002/ajmg.a.61580.

Roerig B, Feller MB. 2000. Neurotransmitters and gap junctions in developing neural circuits. *Brain Res Brain Res Rev*. 32: 86–114.

Schindelin J, Arganda-Carreras I, Frise E, Kaynig V, Longair M, Pietzsch T, Preibisch S, Rueden C, Saalfeld S, Schmid B *et al*. 2012. Fiji: an open-source platform for biological-image analysis. *Nat Methods*. 9:676–682.

Schneggenburger R, Rosenmund C. 2015. Molecular mechanisms governing ca(2+) regulation of evoked and spontaneous release. *Nat Neurosci*. 18:935–941.

Shah MM. 2014. Cortical HCN channels: function, trafficking and plasticity. *J Physiol*. 592:2711–2719.

Simi A, Studer M. 2018. Developmental genetic programs and activity-dependent mechanisms instruct neocortical area mapping. *Curr Opin Neurobiol*. 53:96–102.

Thuault SJ, Malleret G, Constantinople CM, Nicholls R, Chen I, Zhu J, Panteleyev A, Vronskaya S, Nolan MF, Bruno R *et al*. 2013. Prefrontal cortex HCN1 channels enable intrinsic persistent neural firing and executive memory function. *J Neurosci*. 33:13583–13599.

Downloaded from https://academic.oup.com/cercor/article-abstract/doi/10.1093/cercor/bhaa137/5860958 by University of Canberra user on 25 June 2020

Tomassy GS, De Leonibus E, Jabaudon D, Lodato S, Alfano C, Mele A, Macklis JD, Studer M. 2010. Area-specific temporal control of corticospinal motor neuron differentiation by COUP-TFI. *Proc Natl Acad Sci U S A*. 107:3576–3581.

Tritsch NX, Yi E, Gale JE, Glowatzki E, Bergles DE. 2007. The origin of spontaneous activity in the developing auditory system. *Nature*. 450:50–55.

Uhlen P, Fritz N, Smedler E, Malmersjo S, Kanatani S. 2015. Calcium signaling in neocortical development. *Dev Neurobiol*. 75:360–368.

van Welie I, Remme MW, van Hooft JA, Wadman WJ. 2006. Different levels of Ih determine distinct temporal integration in bursting and regular-spiking neurons in rat subiculum. *J Physiol*. 576:203–214.

Wang Z, Xu NL, Wu CP, Duan S, Poo MM. 2003. Bidirectional changes in spatial dendritic integration accompanying long-term synaptic modifications. *Neuron*. 37:463–472.

Wefelmeyer W, Puhl CJ, Burrone J. 2016. Homeostatic plasticity of subcellular neuronal structures: from inputs to outputs. *Trends Neurosci*. 39:656–667.

Williams SR, Stuart GJ. 2000. Site independence of EPSP time course is mediated by dendritic I(h) in neocortical pyramidal neurons. *J Neurophysiol*. 83:3177–3182.

Williams SR, Stuart GJ. 2003. Voltage- and site-dependent control of the somatic impact of dendritic IPSPs. *J Neurosci*. 23:7358–7367.

Yamada R, Kuba H. 2016. Structural and functional plasticity at the axon initial segment. *Front Cell Neurosci*. 10:250.

Yamamoto N, Lopez-Bendito G. 2012. Shaping brain connections through spontaneous neural activity. *Eur J Neurosci*. 35:1595–1604.

Zhang Y, Bonnan A, Bony G, Ferezou I, Pietropaolo S, Ginger M, Sans N, Rossier J, Oostra B, LeMasson G *et al*. 2014. Dendritic channelopathies contribute to neocortical and sensory hyperexcitability in Fmr1(−/y) mice. *Nat Neurosci*. 17:1701–1709.

Zhou D, Lambert S, Malen PL, Carpenter S, Boland LM, Bennett V. 1998. AnkyrinG is required for clustering of voltage-gated Na channels at axon initial segments and for normal action potential firing. *J Cell Biol*. 143:1295–1304.

Downloaded from https://academic.oup.com/cercor/article-abstract/doi/10.1093/cercor/bhaa137/5860958 by University of Canberra user on 25 June 2020